Soft-tissue evidence for homeothermy and crypsis in a Jurassic ichthyosaur

Lindgren, Johan; Sjövall, Peter; Thiel, Volker; Zheng, Wenxia; Ito, Shosuke; Wakamatsu, Kazumasa; Hauff, Rolf; Kear, Benjamin P.; Engdahl, Anders; Alwmark, Carl; Eriksson, Mats E.; Jarenmark, Martin; Sachs, Sven; Ahlberg, Per E.; Marone, Federica; Kuriyama, Takeo; Gustafsson, Ola; Malmberg, Per; Thomen, Aurélien; Rodríguez-Meizoso, Irene; Uvdal, Per; Ojika, Makoto; Schweitzer, Mary H.

Published in:
Nature

DOI:
10.1038/s41586-018-0775-x

2018

Citation for published version (APA):
Lindgren, J., Sjövall, P., Thiel, V., Zheng, W., Ito, S., Wakamatsu, K., Hauff, R., Kear, B. P., Engdahl, A., Alwmark, C., Eriksson, M. E., Jarenmark, M., Sachs, S., Ahlberg, P. E., Marone, F., Kuriyama, T., Gustafsson, O., Malmberg, P., Thomen, A., ... Schweitzer, M. H. (2018). Soft-tissue evidence for homeothermy and crypsis in a Jurassic ichthyosaur. *Nature*, *564*(7736), 359-365. https://doi.org/10.1038/s41586-018-0775-x

Total number of authors:
23

LUND UNIVERSITY

PO Box 117
221 00 Lund
+46 46-222 00 00

Soft tissue evidence for homeothermy and crypsis in a Jurassic ichthyosaur

Johan Lindgren[1], Peter Sjövall[2], Volker Thiel[3], Wenxia Zheng[4,5], Shosuke Ito[6], Kazumasa Wakamatsu[6], Rolf Hauff[7], Benjamin P. Kear[8], Anders Engdahl[9], Carl Alwmark[1], Mats E. Eriksson[1], Martin Jarenmark[1], Sven Sachs[10], Per E. Ahlberg[11,12], Federica Marone[13], Takeo Kuriyama[14,15], Ola Gustafsson[16], Per Malmberg[17], Aurélien Thomen[18], Irene Rodríguez-Meizoso[19], Per Uvdal[20], Makoto Ojika[21] & Mary H. Schweitzer[1,4,5]

[1]Department of Geology, Lund University, 223 62 Lund, Sweden. [2]RISE Research Institutes of Sweden, Chemistry and Materials, 501 15 Borås, Sweden. [3]Geobiology, Geoscience Centre, University of Göttingen, 37077 Göttingen, Germany. [4]Department of Biological Sciences, North Carolina State University, Raleigh, NC 27695, USA. [5]North Carolina Museum of Natural Sciences, Raleigh, NC 27601, USA. [6]Department of Chemistry, Fujita Health University School of Health Sciences, Toyoake, Aichi 470-1192, Japan. [7]Urweltmuseum Hauff, 73271 Holzmaden, Germany. [8]Museum of Evolution, Uppsala University, 752 36 Uppsala, Sweden. [9]MAX-IV laboratory, Lund University, 221 00 Lund, Sweden. [10]Naturkunde-Museum Bielefeld, Abteilung Geowissenschaften, 33602 Bielefeld, Germany. [11]Science for Life Laboratory, Uppsala University, 751 23 Uppsala, Sweden. [12]Department of Organismal Biology, Uppsala University, 752 36 Uppsala, Sweden. [13]Swiss Light Source, Paul Scherrer Institute, 5232 Villigen, Switzerland. [14]Institute of Natural and Environmental Sciences, University of Hyogo, Hyogo 669-3842, Japan. [15]Wildlife Management Research Center, Hyogo 669-3842, Japan. [16]Department of Biology, Lund University, 223 62 Lund, Sweden. [17]Department of Chemistry and Chemical Engineering, Chalmers University of Technology, 412 96 Göteborg, Sweden. [18]Department of Chemistry and Molecular Biology, University of Gothenburg, 405 30 Göteborg, Sweden. [19]Centre for Analysis and Synthesis, Department of Chemistry, Lund University, 221 00 Lund, Sweden. [20]Chemical Physics, Department of Chemistry, Lund University, 221 00 Lund, Sweden. [21]Department of Applied Biosciences, Graduate School of Bioagricultural Sciences, Nagoya University, Nagoya 464-8601, Japan.

Ichthyosaurs are extinct marine reptiles that display a remarkable external similarity to modern toothed whales. Here we show that this resemblance is more than skin deep. We apply a novel multidisciplinary experimental approach to characterise the cellular and molecular composition of integumental tissues in an exceptionally preserved specimen of the Early Jurassic ichthyosaur *Stenopterygius*. Our analyses recovered still flexible remnants of the original scaleless skin, comprising morphologically distinct epidermal and dermal layers. These are underlain by insulating blubber that would have augmented streamlining, buoyancy and homeothermy. Additionally, we identify endogenous proteinaceous and lipid constituents, together with keratinocytes and branched melanophores that contain eumelanin pigment. Distributional variation of melanophores across the body suggests countershading, possibly enhanced by physiological adjustments of colour to enable photoprotection, concealment and/or thermoregulation. Ichthyosaur convergence with extant marine amniotes thus extends to ultrastructural and molecular levels, reflecting the omnipresent constraints for their shared adaptation to pelagic life.

With their dolphin-like external form, the Mesozoic ichthyosaurs are icons of evolution. Although finds from the 18th and 19th centuries pioneered their recognition as prehistoric oceangoing reptiles, it was not until the discovery of articulated skeletons with complete body outlines that the extent of this anatomical specialisation towards an obligate marine existence was fully appreciated. These celebrated specimens from the Holzmaden area of Germany reveal a combination of paired flippers, triangular dorsal fin and lunate tail for efficient hydrodynamic manoeuvring. Derived (parvipelvian) ichthyosaurs were thus remarkably similar in appearance to extant pelagic cruisers, such as odontocete whales and lamnid sharks[1].

Despite this textbook example of evolutionary convergence, the nature of the residues forming the body contours, and the diagenetic processes leading to their preservation, remain incompletely understood. The various competing interpretations include genuine remnant soft parts, comprising either carbonised and/or phosphatised integument and superficial musculature/connective tissue[2,3], *in situ* transformed organic matter, such as adipocere[4,5], or microorganismal replacement structures[1,6]. Creases described as dermal tensile fibres have also been documented[5], but alternatively dismissed as sedimentary cracks and tool marks[7].

Here we use an integrated ultrastructural and molecular investigation of a chemically untreated specimen (MH 432, Urweltmuseum Hauff, Holzmaden, Germany) of the Early Jurassic (Toarcian) parvipelvian *Stenopterygius* to resolve these long-standing contentions. This fossil reveals endogenous cellular, sub-cellular and biomolecular constituents within relict skin and subcutaneous tissue (Figs 1–5 and Extended Data Figs 1–7). A possible internal organ trace, interpreted as the liver, is also documented (Extended Data Fig. 8), together with comparative data obtained from modern marine tetrapods (Extended Data Fig. 9).

The fossil and experimental design

The soft tissue residues of MH 432 comprise a buff-coloured to black coating that adheres to the outside of the postcranium, but also extends some distance beyond the periphery of the bones to produce a bedding-parallel outline of the animal (Fig. 1 and Extended Data Fig. 1a). A second, superficially amorphous material occurs as light beige patches external to this film in the abdominal region (Extended Data Fig. 1b), whereas fibrous matter (Extended Data Fig. 1c) and the red-brown liver trace are located inside the rib cage (Fig. 1 and Extended Data Fig. 1b).

We conducted examinations under regular (Fig. 1a and Extended Data Fig. 1a–c) and ultraviolet (UV) light (Extended Data Fig. 1d–m), as well as through synchrotron rapid-scanning X-ray fluorescence (Fig. 1c and Extended Data Fig. 1n, o). The resulting data served to assess the elemental composition of the soft parts, but were also used to identify suitable areas for in-depth molecular and imaging investigations. Tissue and sediment samples (Fig. 1b) were collected with sterile instruments and distributed to multiple institutions for independent cross-referencing analyses. Some samples were subjected to chemical extraction, while others were first examined untreated, and then again after treatment with ethylenediaminetetraacetic acid (EDTA).

Cutis and melanophores

The soft tissues of the body outline are preserved as a mineralised, semi-continuous covering (Fig. 1 and Extended Data Fig. 1). No scales or scutes are evident (Fig. 2a, b). Instead, the external surface is smooth, and was presumably comparable in life to the rubbery[8,9] skin of extant cetaceans (Fig. 2q) and adult individuals of the leatherback sea turtle, *Dermochelys coriacea* (Fig. 2s). Wrinkles and ripples (Fig. 2c, d) closely resemble those observed to distort decomposing integument following loss of structural integrity (Fig. 2r). Demineralisation and subsequent histological/microscopic examination evinced a multi-layered subsurface architecture (Fig. 2e–p and Extended Data Fig. 2a–e) corresponding to the laminated epidermis and dermis of modern tetrapods[10,11] (Fig. 2t). Sparse oval perforations ~70 μm in diameter pass through the cutis (Fig. 2i, j), and are tentatively interpreted as pores.

The ~100 μm thick epidermis retains cell-like structures that likely represent preserved melanophores (Fig. 3 and Extended Data Fig. 3) and keratinocytes undergoing differentiation[11,12] (Fig. 2m–o). The outer section of the skin can be further divided into an upper stratum corneum, characterised by stratified squamous cells (Fig. 2m–o and Extended Data Fig. 2b), and a deeper unit containing polyhedral to oblate cellular bodies that become increasingly flattened towards the external surface (Fig. 2o and Extended Data Fig. 2d). This lower part is reasonably interpreted as vestiges of the middle and basal layers of the epidermis, comprising the stratum intermedium and stratum germinativum, respectively (the junction between these layers is not well defined in MH 432). Vertical extensions at the epidermal-dermal interface form a regularly arranged series of interlocking ridges that run parallel to the longitudinal axis of the body (Fig. 2f and Extended Data Fig. 2a). This microstructure is consistent with the basement membrane of extant tetrapods[9], and overlies an ~80 μm thick band of connective tissue fibres constituting the superficial dermis (Fig. 2l, p and Extended Data Fig. 2e).

The fossilised pigment cells have long dendritic processes and a granular internal filling (Fig. 3, Extended Data Fig. 3 and Supplementary Video 1). They are virtually identical in size (~10 μm in diameter, excluding the external projections), geometry and inner fabric to the branched melanophores of extant reptiles (Fig. 3l–q). Our chemical identification of eumelanin (Fig. 3r, s and Extended Data Fig. 3f) further suggests that the granular content represents remnant melanosome organelles (see Supplementary Information).

Preservation of cutis

We posit that the cutis of MH 432 was fossilised through partial replication in authigenic calcium phosphate[13] (Fig. 1c and Extended Data Figs 1n, o, 2f, g), an eogenetic mineralisation process that enabled the retention of three-dimensional cellular morphologies. However, our experimental removal of the inorganic phase revealed a second preservational mode: *in situ* molecular transformation (‘geopolymerisation’ or ‘kerogenisation’) – a mechanism whereby labile to relatively recalcitrant organic compounds are altered into stable macromolecules by (re-)polymerisation, polycondensation and/or defunctionalisation reactions[14–16]. Energy-dispersive X-ray microanalysis (EDX), time-of-flight secondary ion mass spectrometry (ToF-SIMS), nanoscale secondary ion mass spectrometry (NanoSIMS), pyrolysis-gas chromatography/mass spectrometry (Py-GC/MS), and infrared (IR) microspectroscopy collectively confirmed the primarily organic composition of the artificially released (and still somewhat flexible; Supplementary Video 2) tissues and cells as being dominated by aliphatic and aromatic hydrocarbons (Fig. 4a and Extended Data Figs 2h, 4a, 5). Such biogeopolymers are likely diagenetic transformation products from a variety of compounds. Although specific precursor molecules are difficult to identify, an endogenous lipid source for at least some of them can be reasonably inferred from the inherent chemical stability of lipid hydrocarbon skeletons, and their demonstrated ability to polymerise *in situ*; this constitutes a major factor in organic preservation[14–16]. Our interpretation is corroborated by the apparent preferential preservation of lipid-rich cellular envelopes[11] (Fig. 2o and Extended Data Fig. 2d), intracellular vacuoles[17] (Fig. 2k) and extracellular lamellar membranes[11] (Fig. 2n and Extended Data Fig. 2b).

Apart from hydrocarbons, traces of the original biomolecular makeup, including cholesterol derivatives (Fig. 4b and Extended Data Fig. 4a) and proteinaceous constituents (Fig. 4a and Extended Data Figs 5a, b, 6) retaining the immunological characteristics of tropomyosin, haemoglobin, α-keratin, elastin, actin, and collagen (Fig. 4e–n and Extended Data Fig. 7a–f), were detected using a combination of ToF-SIMS, Py-GC/MS, amino acid analysis, and *in situ* immunohistochemistry (IHC) incorporating both fluorescence and immunogold labelling. ToF-SIMS and IHC further demonstrated co-localisation of the geochemical signatures within discrete tissue regions (Fig. 4e–n and Extended Data Figs 5a, b, 7a–f). Antibody reactivity showed that the various epitopes were spatially distinct, and thus comparable to immunolabelling patterns produced by artificially matured leatherback sea turtle and harbour porpoise (*Phocoena phocoena*) integuments (Extended Data Figs 7i–t, 9n–q). Significantly, although remnant β-keratin has been previously reported from multimillion-year-old epidermal appendages[18], we were unable to recognise breakdown products of this durable[19] protein (Extended Data Fig. 7g, h). β-keratin is responsible for the development of hard corneous layers in sauropsid claws, scales and scutes[20]. Therefore, its apparent absence in MH 432 supports our microscopy-based observation of a scaleless skin in this ichthyosaur.

Blubber

The subcutaneous layer of MH 432 is >500 μm thick and comprises a glossy black material superimposed over a fibrous mat (Fig. 5a). Histological and chemical analysis showed vertical stratification into a dense, indistinctly laminated carbonaceous unit sandwiched between two sets of surface-parallel seams that are enriched in calcium phosphate (Fig. 5b–f, l, m and Extended Data Fig. 5c). The dark matter is dominated by aliphatic and aromatic compounds (Fig. 5i–n), and appears to represent a highly condensed tissue residue, in which biogeopolymers are so abundant that they obscure virtually all microstructural details when inspected under TEM (Fig. 5e, f). This compares well with previously documented fossilised lipid-rich source structures[14–16]. Moreover, our artificial maturation of harbour porpoise integument (Extended Data Fig. 9e–q) demonstrates that blubber – the peripherally distributed fibro-adipose tissue layer that until now only has been identified in modern cetaceans, sirenians, pinnipeds, and the leatherback sea turtle[21,22] – converts into a similarly condensed mass of flattened cells and fibre bundles when subjected to elevated pressure and temperature (the epidermis was otherwise relatively unaffected by these experimental procedures; Extended Data Fig. 9f–i). Based on its anatomical localisation, chemical composition and fabric, we therefore interpret the subcutaneous material in MH 432 as most probably representing fossilised blubber. Support for this hypothesis includes the presence of potential fatty acid moieties (Extended Data Fig. 4b), as well as the calcium phosphate-reinforced seams (Fig. 5c, d, l, m and Extended Data Fig. 5c), which correspond anatomically to the reticular dermis and superficial fascia of extant balaenid[10] and odontocete[9] whales. These connective tissue layers consist of closely spaced collagen and elastin strands that enclose the more fat-laden parts of the blubber. Although integumental fibrillar proteins do not normally biomineralise[23], they do possess an inherent ability to bind calcium and phosphate ions[24], and thus could feasibly have induced the nucleation of calcium phosphate nano-crystallites during the eogenesis of MH 432.

Due to taphonomic overprinting, the original thickness of the blubber in MH 432 is difficult to estimate. However, it must have been considerable based on comparisons with our experimental reduction of a 20 mm thick blubber layer from a 1.24 m long harbour porpoise to less than 250 μm under artificially created diagenetic conditions (Extended Data Fig. 9e–j).

Implications

Existing evidence indicates that ichthyosaurs were predominantly dark-coloured in life[2,3,25], much like most air-breathing vertebrates that today inhabit pelagic environments[8,26,27]. More elaborate patterns involving multiple biochromes and/or photonic nanostructures have been proposed[28], but are inconsistent with fossil data[2,3,25], as well as the conservative skin palette found in extant oceanic amniotes[8,27]. Conversely, the conspicuous abundance of melanophores across the flank of MH 432 (Fig. 2g) contrasts with their absence in the belly region (Fig. 2i), providing compelling evidence that this individual was originally countershaded. A distributional differentiation of dark and light melanin-based colours between the dorsal and ventral surfaces of the body occurs in many seagoing tetrapods[8,27], and functions to provide camouflage[29], protect against UV radiation during sea-surfacing behaviours[30], and/or confer thermoregulatory advantages in cold climates[31]. Conflicting reports[2,25] of monotonal schemes in smaller-bodied individuals of *Stenopterygius* might indicate ontogenetic changes in colour comparable to those seen in living sea turtles[26]. Moreover, our identification of branched melanophores hints at the possibility that ichthyosaurs were able to physiologically adjust their skin tone via redistribution of melanosomes[12], perhaps to enable UV filtration, concealment, or enhance body temperature stability.

Our morphological and chemical detection of blubber – a hallmark of warm-blooded marine amniotes[21] – provides a rare window into the level of aquatic adaptation achieved by derived ichthyosaurs. In extant animals, blubber accentuates streamlining, buoyancy, and serves as a fat store that can be metabolised during periods of energetic stress[21,22]. However, its primary role as an insulator is crucial to overcome the thermal conductivity of seawater[21], and concurs with reconstructions of ichthyosaurs as homeotherms or regional endotherms[4,32,33]. Suggestions that these ancient reptiles were capable of mesopelagic deep-diving[1], sustained cruising[1], and toleration of cold water environments[34], are likewise accordant with the development of blubber as one of many integrated physiological and behavioural mechanisms required to maintain a high ambient-independent body temperature[4,25,32,34].

Our rigorous experimental results demonstrate that the integument of *Stenopterygius* had both a smooth external surface and thick subcutaneous layer of fibro-adipose tissue. This is strikingly similar to modern whales[9,10], as well as adult individuals of the leatherback sea turtle[8], and reveals multiple aspects of soft tissue convergence ranging across a time span of more than 180 million years. In addition, the cetacean/reptilian trait mosaic of *Stenopterygius* recurs in its integumental histology, with our identification of branched melanophores (as opposed to mammalian melanocytes), and the absence of dermal ossifications (otherwise present in the leatherback sea turtle[8]). We attribute these adaptive specialisations to the commonality of morphological and physiological constraints imposed upon all pelagic tetrapods during their evolutionary transition towards life in the sea.

METHODS

Fossil material. Prior to analysis, MH 432 was rinsed multiple times with 96% ethanol and Milli-Q water to remove potential contaminants from human handling. Tissue and sediment samples were collected from the fossil using sterile instruments and washed successively in 96% ethanol and Milli-Q water. They were subsequently dried under a hood, wrapped loosely in aluminium foil, and stored in sealed, sterile containers. Samples selected for LM, FEG-SEM, TEM, ToF-SIMS, and IR microspectroscopy were demineralised using EDTA (0.5 M, pH 8.0) for about four weeks with regular buffer changes to dissolve the mineral phase. Debris from the demineralisation process was rinsed multiple times with Milli-Q water to discard remaining EDTA. Fresh aluminium foil was used to cover all work areas, and surgical gloves were worn during all handling and treatment. Experimental parameters between ancient and modern (see below) materials were identical; however, both sets of samples were treated in segregated laboratory spaces.

Modern reference materials. Frozen tissue samples from a sub-adult male harbour porpoise, *Phocoena phocoena* (A2016/05526), found dead in Swedish waters in 2016, were provided by the Department of Environmental Research and Monitoring, Environmental Specimen Bank, Swedish Museum of Natural History, Stockholm, Sweden. Similarly, integumental samples from a juvenile male short-beaked common dolphin, *Delphinus delphis* (SAM M26880), washed up dead in South Australia in 2012, were obtained from the South Australian Museum (SAM), Adelaide, Australia. A juvenile leatherback sea turtle, *Dermochelys coriacea* (ZMUC-R2106), stored in 70% ethanol, was acquired as a gift from 'Danmarks Akvarium' in 1962, and has since been part of the vertebrate collection at the Zoological Museum, Natural History Museum of Denmark (ZMUC), Copenhagen, Denmark. The beached carcass of a second (adult female) *D. coriacea* (ZMUC-R2112) was recovered in Denmark in 1979. The integument from ZMUC-R2112 was cleaned and dried, and is currently housed in the collections at the ZMUC.

Maturation experiments. Integument samples from the juvenile leatherback sea turtle (Extended Data Fig. 9a) and harbour porpoise (Extended Data Fig. 9e) were placed in cylindrical borosilicate glass vials with the epidermis facing downwards. The samples were then pressed from the hypodermis side using glass rods with flattened ends that were inserted into the vials. Each vial was placed in a larger beaker, and another smaller beaker (containing 600 g sand) was placed on top of the glass rod to compact the integument. The whole apparatus was placed in a ventilated oven heated to 80°C. The samples were inspected at regular intervals (after 4 h on the first day, and then once on each following day), and the colourless oil expelled from the porpoise blubber was removed using a glass pipette. The samples were heated in this same manner for six consecutive days, during which the fatty inner tissues were compressed into a brittle amber-coloured substance (the epidermis was otherwise only slightly transformed by this same treatment; Extended Data Fig. 9f, g).

To artificially accelerate the maturation process, we also exposed the samples to higher temperatures and pressures. Each compacted sample was first cut into four smaller sections, with one wrapped in aluminium foil and then placed in an autoclave. The autoclave consisted of a stainless-steel high-pressure vessel (30 × 10 mm column, Applied Porous Technologies, Connecticut, USA) connected to an argon gas cylinder. The autoclave was purged three times by filling it to 80 bar with argon gas, before being relieved through the exhaust pipe. The autoclave was subsequently filled to approximately 75% of the desired final pressure, and heated in a thermostat-controlled oven (GC oven, 5890 series II, Hewlett Packard, California, USA). After a few minutes (when the system had reached the desired temperature), a manual valve was used to adjust the final pressure to 200 bar. The samples were first exposed to 100°C and 200 bar for 24 h, and then to 150°C and 200 bar for 96 h; this second exposure was necessary because no further morphological changes were apparent after treatment at 100°C/200 bar. These procedures were found to darken the porpoise blubber (Extended Data Fig. 9h). Sample sections exposed to 200°C and 200 bar for 24 h either disintegrated completely, or turned into a sticky semi-solid substance, which was not examined further.

Light Microscopy (LM). Tissue samples from our comparative selection of extant animals were inundated in freshly prepared fixative solution, 2% paraformaldehyde and 2.5% glutaraldehyde in 0.1 M cacodylate buffer (pH 7.4) for 24 h at 4°C. The samples were then dehydrated in a graded ethanol series and embedded in epoxy resin (Agar 100, Resin kit R1031) via acetone, which was left to polymerise for 48 h at 60°C. The demineralised fossil tissue was immersed in epoxy resin (AGAR 100, Resin kit R1031), which was left to polymerise at room temperature for 72 h, followed by 48 h at 60°C. Semi-thin (1.5 µm) light microscopic (LM) sections were then cut with a glass knife using a Leica EM UC7 Ultramicrotome, and mounted on objective glasses. Every second section was stained with Richardson's solution prior to examination using an Olympus CX21 microscope. Micrographs were recorded using a Lumenera Infinity 2-1RC CCD camera with Lumenera Infinity Analyze version 6.4.1 software.

Field emission gun scanning electron microscopy (FEG-SEM) and energy-dispersive X-ray microanalysis (EDX). Untreated and demineralised fossil samples were mounted on either conductive tape, sterile silicon wafers, or CaF_2 infrared windows. Following ToF-SIMS and/or IR microspectroscopic measurements (see below), the samples were coated with gold or platinum/palladium using a Cressington 208HR High Resolution Sputter Coater. They were then studied in a Tescan Mira3 High Resolution Schottky FEG-SEM with both standard and in-lens secondary electron and backscattered electron detectors at acceleration voltages between 1 and 15 kV, and a working distance of 3–10 mm. Elemental analyses and mappings were performed with an energy-dispersive spectrometer (X-MaxN 80, 124 eV, 80 mm^2) from Oxford Instruments, linked to the instrument. Additional investigations were conducted on gold/palladium-coated samples in a Zeiss Supra 40VP FEG-SEM (2 keV electron energy, 3–5 mm working distance, Everhart-Thornley secondary electron detector).

Transmission electron microscopy (TEM). Tissue samples from our comparative selection of extant animals were fixed and embedded in epoxy resin as described above (LM section). Ultra-thin (50 nm) sections were cut using a Leica EM UC7 Ultramicrotome equipped with a diamond knife, and mounted on pioloform-coated copper grids without further treatment or staining. Demineralised fossil tissue was likewise embedded in epoxy resin (see LM section). Ultra-thin (50 nm) sections were cut and mounted on copper grids without further treatment or staining. All sections were examined in a JEOL JEM-1400 PLUS TEM at 100 kV. Micrographs were recorded with a JEOL Matataki CMOS camera using TEM Centre for JEM1400 Plus software.

***In situ* immunohistochemistry (IHC).** Extant animal and demineralised fossil tissues were embedded in LR White (hard grade, EMS, Cat# 14383) according to manufacturer specifications. 200 nm sections were taken on a Leica EM UC6 Ultramicrotome for *in situ* IHC, whereas 90 nm sections were used for post-embedding TEM immunogold labelling. The 200 nm sections were transferred to 6-well Teflon-coated slides and dried before being etched with 25 µg/ml proteinase K, and 0.5 M EDTA for epitope retrieval. This was followed by incubation in 1 mg/ml sodium borohydride to quench autofluorescence. Non-specific binding was prevented by incubating sections in 4% normal serum prior to immune labelling with each primary antibody overnight at 4°C; working dilutions followed specifications recommended by the manufacturers. After repeated washing to remove unbound antibodies, the sections were incubated with a biotin-conjugated secondary antibody for 2 h at room temperature. An avidin-biotin reagent (Vector Laboratories A-2001) was applied for 1 h. All incubations were separated by sequential washes using ×1 PBS. Finally, all of the sections were mounted with anti-fade mounting medium (Vector H-1000), and coverslips were applied. Examinations were undertaken using a Zeiss Axioskop 2 Plus biological microscope.

Immunogold assays were performed at room temperature on both the extant and fossil tissue samples. The fossil tissues were prepared in a specifically designed laboratory in which no modern animal tissues are permitted; conversely, the extant animal samples were prepared in a separate laboratory. Sections of 90 nm thickness were collected on carbon-coated nickel grids (EMS, Cat# CFT200-NI). The grids were then incubated in: (1) PBS buffer with 1% Tween20 for 10 min; (2) 4% donkey serum in PBS (1 h); (3) primary antibodies against α-keratin (1:10) for 3 h; (4) washed with PBS buffer with 1% Tween20 10 times; and (5) 18 nm Colloidal Gold AffiniPure Donkey Anti-Goat IgG (H+L) 1:10 (Jackson Immuno Research Inc., Cat# 705-215-147). After incubation with primary antibodies, the grids were washed using the procedures outlined above, and then stained in methanolic uranyl acetate followed by Reynold's lead citrate, and inspected using an aberration corrected STEM-FEI Titan 80-300 electron microscope.

Synchrotron-radiation X-ray tomographic microscopy (SRXTM). SRXTM was performed at the TOMCAT beamline of the Swiss Light Source, Paul Scherrer Institute, Switzerland. Samples were mounted on either low light refractive 0.30 mm fishing lines (Berkley, Trilene super strong, 100% fluorocarbon) or wooden toothpicks. The beam energy was set to 12 and 20 keV depending on sample size. The transmitted X-rays were converted into visible light by a 5.9 µm thick Tb-doped LSO scintillator screen (FEE, Germany). Projection images (1,200 over 180°) were magnified by microscope optics (×40) and digitised by a sCMOS camera (PCO.edge 5.5) with a 2,560 × 2,160 pixel chip, a 6.5 µm pitch, and 16 bit dynamic range. Tomographic reconstructions followed single distance phase retrieval of the acquired projections, and were performed using a Fourier transform method routine, and a gridding procedure. The resulting tomographic volumes had an isotropic voxel size of 0.16 µm, and were rendered using Voxler 2 and 3.

Synchrotron rapid-scanning X-ray fluorescence imaging (SRS-XRF). X-ray fluorescence images were collected at the Stanford Synchrotron Radiation Lightsource (SSRL) using beamline 10-2. The incident X-ray energy was set to 11.0 keV using a Si (111) double crystal monochromator with the Stanford Positron Electron Accelerating Ring (SPEAR) storage ring containing 500 mA at 3.0 GeV. The fluorescence lines of the targeted elements, as well as the intensity of the total scattered X-rays, were monitored using a silicon drift Vortex detector (SII NanoTechnology USA Inc.). The focused beam of 100 × 100 µm was determined by a 100 µm Ta pinhole aperture. The incident and transmitted X-ray intensities were measured with nitrogen-filled ion chambers, and the incident X-ray flux on the sample was measured at ~8e10 ph/s. The samples were mounted at 45° relative to the incident X-ray beam, with the fluorescence detector mounted at 90° relative to the incident beam. The sample and detector were maintained within an ambient atmospheric environment, with the detector held at a distance of ~4 cm from the sample. The samples were mounted vertically on an aluminium bracket, and spatially rastered in the X-ray beam while data were collected continuously during stage motion. The fluorescence signal was gated by the encoder signal at pixel sizes of either 100 or 200 µm. Beam exposure time was 20 ms per pixel.

Infrared (IR) microspectroscopy. IR microspectroscopic measurements were recorded at the Department of Biology, Lund University, Sweden. A Hyperion 3000 microscope combined with a Tensor 27 spectrometer were used, together with either a single element mercury cadmium telluride (MCT) detector (250 × 250 µm) or a 64 × 64 pixel Focal Plane Array (FPA) detector and a Globar light source. The microscope was operated in transmission mode at 4 cm^{-1} resolution, and a ×15 objective was employed. 128 individual scans were averaged to achieve a good signal-to-noise ratio. Sample 13 (which includes the isolated melanophore depicted in Fig. 3e–g and Extended Data Fig. 3d, g) was also analysed at the SMIS beamline, Synchrotron SOLEIL, in France. This facility uses an Agilent Cary 620 FTIR Microscope system with a 128 × 128 FPA MCT detector (4 cm^{-1} resolution, ×25 objective).

Nanoscale secondary ion mass spectrometry (NanoSIMS). Ion images were acquired using the Cameca NanoSIMS 50L instrument at the Chemical Imaging Infrastructure, Chalmers University of Technology and University of Gothenburg, Sweden. Measurements were performed with a 16 keV Cs^+ primary ion beam, rastering the sample surface using a 1.5 pA (aperture diaphragm D1 2) primary current. The spatial resolution of the primary beam size was 200 nm. The count rates of the $^{12}C^{1}H^{-}$, $^{12}C^{14}N^{-}$, $^{28}Si^{-}$, $^{31}P^{-}$, ^{32}S, and $^{40}Ca^{16}O^{-}$ were measured simultaneously in multicollection mode using electron multipliers. Mass-filtered images were then acquired using entrance slit 3 (width, 20 µm) and aperture slit 2 (width, 200 µm); the energy slit was kept fully open (energy band pass, ≤100 eV). The relative transmission of the mass spectrometer is ~38% with a mass resolving power of 9,000 on $^{28}Si^{-}$ (CAMECA definition). Each image is composed of 10 planes (for each measured mass). Images were processed using ImageJ and the OpenMIMS plugin. The count rates were corrected using a dead time of 44 ns for each electron multiplier.

Time-of-flight secondary ion mass spectrometry (ToF-SIMS). ToF-SIMS analyses were conducted in the static SIMS mode on a TOFSIMS IV instrument (IONTOF GmbH) using 25 keV Bi_3^+ primary ions and low energy electron flooding for charge compensation. Positive and negative ion data were acquired with the instrument optimised for either high mass resolution ($m/\Delta m$ ~5,000, spatial resolution ~3–4 µm) or high image resolution ($m/\Delta m$ ~300, spatial resolution ~0.2–0.5 µm), because these properties cannot be optimised simultaneously without inordinate increases in analysis time[35]. The pulsed primary ion current was set at 0.10 pA for the high mass resolution data, and 0.04 pA for the high image resolution data.

Pyrolysis-gas chromatography/mass spectrometry (Py-GC/MS). Untreated fossil and sediment samples were ground to powder and loaded on a fast-heating Pt-filament of a Pyrola 2000 device (Pyrolab SB, Sweden) coupled to a Varian CP3800 GC and a Varian 1200L MS. Two GC/MS runs were conducted on each sample. Firstly, the filament was heated in 2 ms from 200 to 330°C (hold 40 s), and a GC/MS run was performed to record the resulting volatile bitumen compounds and contaminants (if present). The sample remained in the pyrolysis device throughout the duration of this first run. In the second run, the temperature was increased to 560°C (hold 10 s) within 2 ms to release moieties that were tightly bound to the organic matter (largely in insoluble kerogen; runs shown in Fig. 4b and Extended Data Fig. 4). Samples were weighed onto the pyrolysis filament (~5 mg for each run). As a monitor of system performance, 40 ng of perdeuterated *n*-icosane ($C_{20}D_{42}$; Sigma) dissolved in 4 μL *n*-hexane was added to each sample. Here we figure pyrograms that exhibited high transfer efficiency consistent with the standard (Fig. 4b and Extended Data Fig. 4). Chromatograms were normalised to the sample weight loaded onto the pyrolysis filament (Fig. 4b and Extended Data Fig. 4b), or adjusted to the highest *n*-alkane peak to illustrate the abundance of the key compound, 5α,14α,17α(H)-cholestane 20R, relative to other pyrolysis products (Extended Data Fig. 4a). This molecule was identified by comparison against, and co-injection of, a commercially available standard (Chiron Laboratories AS). Identification of the 20S isomer was based on its retention time and mass spectral characteristics; minor co-elution with other isomers may have occurred. The GC was equipped with a Phenomenex Zebron ZB-5 capillary column (30 m, 0.1 μm film thickness, inner diameter 0.25 mm), and used helium (1.7 mL/min) as the carrier gas. Pyrolysis products were flushed onto the GC column at an injector temperature of 300°C, and a split rate of 20. The GC oven temperature was ramped from 40 (3 min) to 310°C at 10°C min^{-1}, and held for 15 min. Electron ionisation mass spectra were recorded at 70 eV in full scan mode (mass range 50–450, scan time 0.35 s).

Alkaline hydrogen peroxide oxidation (AHPO). Untreated fossil and sediment samples were mechanically ground into a powder. Approximately 2–6 mg of each sample was heated with 500 μL 6 M HCl at 110°C for 16 h in a 10 ml test tube. Following addition of 1 mL water, the tube was centrifuged at 14,000 g for 10 min, and the residue then washed with 1 mL water and subjected to AHPO[36]. 100 μL water, 375 μL 1 M K_2CO_3 and 25 μL 30% H_2O_2 were added to each tube. Following vigorous mixing at 25°C for 20 h, the residual H_2O_2 was decomposed by adding 50 μL 10% Na_2SO_3, and the resulting mixture acidified with 140 μL 6 M HCl. The oxidation mixture was centrifuged at 10,000 g for 1 min, and an aliquot (80 μL) of the supernatant was injected directly into a high-performance liquid chromatography (HPLC) system. The setup included a JASCO 880-PU liquid chromatograph (JASCO Co., Tokyo, Japan), a Shiseido C18 column (Capcell Pak, Type MG; 4.6 × 250 mm; 5 μm particle size; Shiseido, Tokyo, Japan), and a JASCO UV detector, which was monitored at 269 nm. The mobile phases comprised 0.1 M potassium phosphate buffer (pH 2.1): methanol, 99:1, at 45°C for pyrrole-2,3,5-tricarboxylic acid (PTCA) and pyrrole-2,3-dicarboxylic acid (PDCA) and 0.4 M HCOOH: methanol, 85:15, at 35°C for PTCA and pyrrole-2,3,4,5-tetracarboxylic acid (PTeCA).

Amino acid analysis. Powdered samples (~6–10 mg) were placed in vacuum hydrolysis test tubes (Kontes Glass, # 896860-8910), and 1 mL 6 M HCl containing 1% phenol was added to each tube. The tubes were then evacuated, sealed, and placed in an oil bath at 110°C for 24 h. The hydrolysates were extracted twice with 2 mL ether, and evaporated to dryness under vacuum. The residues were then dissolved in 200–400 μL 0.1 M HCl, and centrifuged at 10,000 g. Aliquots (4–5 μL) were applied to LC/MS for quantitative amino acid analysis. Two solvent systems (condition I and II) were used because of variable amino acid sensitivity: condition I for alanine, glutamic acid, glycine, and serine; condition II for all other amino acids. Standard amino acid solutions of 10 and 50 μM in 0.1 M HCl were employed as references. Liquid chromatographic (LC) conditions included an Agilent 1200 HPLC system (Hewlett Packard, Palo Alto, USA) with an Intrada Amino Acid (2 × 75 mm) (Imtakt, Kyoto, Japan) column, and a sequence of solvents: (condition I) A = MeCN-THF-25 mM $HCOONH_4$-HCOOH (9:75:16:0.3), B = MeCN-100 mM $HCOONH_4$ (20:80), 0% B (0–7 min), 0–17% B (7–21 min), 100% B (21–35 min); (condition II) A = MeCN-HCOOH (100:0.1), B = 100 mM $HCOONH_4$, 15% B (0–3 min), 15–100% B (3–20 min), 100% B (20–24 min). The flow rate was set at 0.2 mL/min. MS conditions incorporated a HCTplus (Bruker Daltonics, Billerica, MA, USA) with an ESI positive source, an ionisation nebulizer at 30 psi, dry gas at 7.0 L/min, dry temperature at 320°C, and an ion trap analyser.

Statistics and reproducibility. 41 samples were collected from MH 432 and its associated matrix (Fig. 1b); 18 of these were demineralised. All samples were photographically documented (Figs 2e–i, 3a–c, 5a and Extended Data Fig. 2a), together with comparative tissues from extant vertebrates (Fig. 2q–s and Extended Data Fig. 9e). The following experiments were repeated independently with similar results: LM (histological sections): MH 432 (Figs 2l, 4c, 5b, i and Extended Data Figs 8b, 10d) nine samples, *Dermochelys* (Figs 2t, 3l–n and Extended Data Fig. 9a–

d) nine samples, *Phocoena* (Extended Data Fig. 9g, i, j) six samples; FEG-SEM: MH 432 (Figs 2j, k, m, p, 3e–g, 5c and Extended Data Figs 3b, c, 8c, d) eight samples; EDX: MH 432 (Fig. 5d and Extended Data Figs 2f, g, 3d) eight samples; TEM: MH 432 (Figs 2n, o, 3h–j, 5e, f and Extended Data Figs 2b–e, 8i, j, 10e–h, j) nine samples, *Dermochelys* (Fig. 3o–q,) nine samples, *Phocoena* (Extended Data Fig. 9k–m) six samples; IHC: Fig. 4e–n (MH 432 Sample 13: tropomyosin four times, ostrich haemoglobin four times, alligator haemoglobin three times; MH 432 Sample 8: α-keratin four times; MH 432 Sample 12: immunogold α-keratin three times), Fig. 5g, h (Sample 13a: α-keratin two times), Extended Data Fig. 7 (MH 432 samples 8 and 12a: elastin two times, actin three times, collagen two times, β-keratin two times; *Dermochelys*: tropomyosin two times, collagen two times, alligator haemoglobin two times, ostrich haemoglobin two times, α-keratin four times, immunogold α-keratin three times), Extended Data Fig. 8e–h (MH 432 Sample 7: ostrich haemoglobin four times, alligator haemoglobin three times); SRXTM: (Fig. 3d and Extended Data Fig. 3a) five times; IR microspectroscopy: the intensity map (Fig. 5j) was generated from 128 individual scans, each spectrum in Fig. 5k represents an average of three spots, the melanophore spectrum (Extended Data Fig. 3g) is an average of 32 individual scans (repeated twice); NanoSIMS: melanophore (Fig. 3k and Extended Data Fig. 3e) six times, LM section (Fig. 4d and Extended Data Fig. 2h) four times; ToF-SIMS: eumelanin identification (Fig. 3s) four times, PAH and peptide/protein identification (Fig. 4a and Extended Data Fig. 5a, b) nine times, blubber (Fig. 5l–m and Extended Data Fig. 5c) four (positive ions) and six (negative ions) times, respectively, liver (Extended Data Fig. 8k) six times; Py-GC/MS (Fig. 4b and Extended Data Fig. 4) three (integument, liver and sediment) and four (remote sediment) times; AHPO: (Fig. 3r and Extended Data Fig. 3f) two (liver, belly skin and sediment) and three (flank skin) times (data in Fig. 3r are centre values with standard error of mean); AAA: (Extended Data Fig. 6 and Table S2) two times. The other experiments, including the SRS-XRF mapping (Fig. 1c and Extended Data Fig. 1n, o), UV imaging (Extended Data Fig. 1d–m), maturation experiments (Extended Data Fig. 9b, f–q), and TEM of bacteria (Extended Data Fig. 10i), were not repeated.

Data Availability The *Stenopterygius* specimen examined in this study (MH 432) is permanently accessioned into the collections of Urweltmuseum Hauff, Holzmaden, Germany. The data supporting our findings are available from the corresponding author upon reasonable request.

1. Motani, R. Evolution of fish-shaped reptiles (Reptilia: Ichthyopterygia) in their physical environments and constraints. *Annu. Rev. Earth Planet. Sci.* **33,** 395–420 (2005).
2. Fraas, E. Ueber die Finne von *Ichthyosaurus*. *Jahresh. Vereins vaterl. Naturk. Württemberg* **44,** 280–303 (1888).
3. Whitear, M. On the colour of an ichthyosaur. *Ann. Mag. Nat. Hist.* **9,** 742–744 (1956).
4. Wiman, C. Über Ichthyosaurier und Wale. *Senckenbergiana* **27,** 1–11 (1946).
5. Lingham-Soliar, T. Rare soft tissue preservation showing fibrous structures in an ichthyosaur from the Lower Lias (Jurassic) of England. *Proc. R. Soc. Lond. B* **266,** 2367–2373 (1999).
6. Martill, D. M. Prokaryote mats replacing soft tissues in Mesozoic marine reptiles. *Mod. Geol.* **11,** 265–269 (1987).
7. Smithwick, F. M., Mayr, G., Saitta, E. T., Benton, M. J. & Vinther, J. On the purported presence of fossilized collagen fibres in an ichthyosaur and a theropod dinosaur. *Palaeontology* **60,** 409–422 (2017).
8. Wyneken, J. in *The leatherback turtle: biology and conservation*. 32–48 (John Hopkins University Press, 2015).
9. Cozzi, B., Huggenberger, S. & Oelschläger, H. *Anatomy of Dolphins: Insights into Body Structure and Function* (Academic Press, 2017).
10. Reeb, D., Best, P. B. & Kidson, S. H. Structure of the integument of southern right whales, *Eubalaena australis*. *Anat. Rec.* **290,** 596–613 (2007).
11. Landmann, L. in *Biology of the integument*. 150–187 (Springer, 1986).
12. Alibardi, L. Ultrastructural features of skin pigmentation in the lizard *Heloderma suspectum* with emphasis on xanto-melanophores. *Acta Zool.* **96,** 154–159 (2015).
13. Wilby, P. R. & Briggs, D. E. G. Taxonomic trends in the resolution of detail preserved in fossil phosphatized soft tissues. *Geobios* **20,** 493–502 (1997).

14. Gupta, N. S., Tetlie, O. E., Briggs, D. E. G. & Pancost, R. D. The fossilization of eurypterids: a result of molecular transformation. *Palaios* **22,** 439–447 (2007).
15. Gupta, N. S., Cody, G. D., Tetlie, O. E., Briggs, D. E. G. & Summons, R. E. Rapid incorporation of lipids into macromolecules during experimental decay of invertebrates: initiation of geopolymer formation. *Org. Geochem.* **40,** 589–594 (2009).
16. O'Reilly, S., Summons, R., Mayr, G. & Vinther, J. Preservation of uropygial gland lipids in a 48-million-year-old bird. *Proc. R. Soc. B* **284,** 20171050 (2017).
17. Jackson, M. K. & Sharawy, M. Lipids and cholesterol clefts in the lacunar cells of snake skin. *Anat. Rec.* **190,** 41–46 (1978).
18. Pan, Y. *et al.* Molecular evidence of keratin and melanosomes in feathers of the Early Cretaceous bird *Eoconfuciusornis*. *Proc. Natl. Acad. Sci.* **113,** E7900–E7909 (2016).
19. Moyer, A. E., Zheng, W. & Schweitzer, M. H. Keratin durability has implications for the fossil record: results from a 10 year feather degradation experiment. *PLoS ONE* **11,** e0157699 (2016).
20. Alibardi, L. Soft epidermis of a scaleless snake lacks beta-keratin. *Eur. J. Histochem.* **51,** 145–151 (2007).
21. Iverson, S. J. in *Encyclopedia of marine mammals*. 115–120 (Academic Press, 2009).
22. Davenport, J. *et al.* Fat head: an analysis of head and neck insulation in the leatherback turtle (*Dermochelys coriacea*). *J. Exp. Biol.* **212,** 2753–2759 (2009).
23. Fartasch, M., Haneke, E. & Hornstein, O. P. Mineralization of collagen and elastin fibers in superficial dystrophic cutaneous calcification: an ultrastructural study. *Dermatologica* **181,** 187–192 (1990).
24. Balakrishnan, S. *et al.* Studies on calcification efficacy of stingray fish skin collagen for possible use as scaffold for bone regeneration. *Tissue Eng. Regen. Med.* **12,** 98–106 (2015).
25. Lindgren, J. *et al.* Skin pigmentation provides evidence of convergent melanism in extinct marine reptiles. *Nature* **506,** 484–488 (2014).
26. Wyneken, J. *The Anatomy of Sea Turtles*. U.S. Department of Commerce NOAA Technical Memorandum NMFS-SEFSC-470 (2001).
27. Shirihai, H. & Jarrett, B. *Whales, Dolphins, and Other Marine Mammals of the World* (Princeton University Press, 2006).
28. Vinther, J. A guide to the field of palaeo colour: melanin and other pigments can fossilise: reconstructing colour patterns from ancient organisms can give new insights to ecology and behaviour. *BioEssays* **37,** 643–656 (2015).
29. Marshall, J. & Johnsen, S. in *Animal camouflage, mechanisms and functions*. 186–211 (Cambridge University Press, 2011).
30. Martinez-Levasseur, L. M. *et al.* Acute sun damage and photoprotective responses in whales. *Proc. R. Soc. B* **278,** 1581–1586 (2011).
31. James, M. C., Myers, R. A. & Ottensmeyer, C. A. Behaviour of leatherback sea turtles, *Dermochelys coriacea*, during the migratory cycle. *Proc. R. Soc. B* **272,** 1547–1555 (2005).
32. Bernard, A. *et al.* Regulation of body temperature by some Mesozoic marine reptiles. *Science* **328,** 1379–1382 (2010).
33. Nakajima, Y., Houssaye, A. & Endo, H. Osteohistology of the Early Triassic ichthyopterygian reptile *Utatsusaurus hataii*: implications for early ichthyosaur biology. *Acta Palaeontol. Pol.* **59,** 343–352 (2014).
34. Kear, B. P. Marine reptiles from the Lower Cretaceous of South Australia: elements of a high-latitude cold-water assemblage. *Palaeontology* **49,** 837–856 (2006).
35. Thiel, V. & Sjövall, P. in *Principles and practice of analytical techniques in geosciences*. 122–170 (The Royal Society of Chemistry, 2015).
36. Ito, S. *et al.* Acid hydrolysis reveals a low but constant level of pheomelanin in human black to brown hair. *Pigment Cell Melanoma Res.* **31,** 393–403 (2018).

Supplementary Information is linked to the online version of the paper at www.nature.com/nature.

Acknowledgements We thank Elena R. Schroeter for scientific advice. Samuel M. Webb and Courtney Roach assisted during the SRS-XRF analysis. Tomas Wigren produced the artistic reconstructions. Financial support was provided by a Grant for Distinguished Young Researchers (642-2014-3773, Swedish Research Council) to J.L., as well as a National Science Foundation INSPIRE grant (EAR-1344198) to M.H.S. and W.Z., and donations from Franklin M. and Susan Packard Orr, and Vance and Gail Mullis. The Paul Scherrer Institute, Switzerland, provided beamtime at the TOMCAT beamline of the Swiss Light Source. SRS-XRF data were collected at the Stanford Synchrotron Radiation Lightsource using beamline 10-2. Part of this work was performed at the Analytical Instrumentation Facility (AIF) of North Carolina State University. AIF is supported by the State of North Carolina and the National Science Foundation (ECCS-1542015), and is a member of the North Carolina Research Triangle Nanotechnology Network, a site within the National Nanotechnology Coordinated Infrastructure.

Author contributions J.L. conceived the project. The text was written by J.L. and B.P.K. with contributions from S.S., P.S., M.H.S., and P.E.A., and feedback from all authors. All figures were assembled by J.L. with input from all authors. R.H. collected and prepared MH 432. J.L., P.S. and M.J. recorded the SRS-XRF measurements, O.G., P.S., C.A., T.K., and J.L. conducted the FEG-SEM and TEM analyses, V.T. performed the Py-GC/MS experiments, S.I. and K.W. carried out the AHPO analysis, M.H.S. and W.Z. conducted the IHC investigation, P.S. and J.L. performed the ToF-SIMS experiments, A.T., P.M., J.L., and P.S. carried out the NanoSIMS analysis, A.E., J.L. and P.U. recorded the IR microspectroscopic measurements, M.E.E. and F.M. acquired the SRXTM data, M.O. performed the amino acid analysis, and M.J. and I.R.-M. conducted the maturation experiments.

Author information

Reprints and permissions information is available at www.nature.com/reprints.
The authors declare no competing interests.
Correspondence and requests for materials should be addressed to J.L. (johan.lindgren@geol.lu.se)

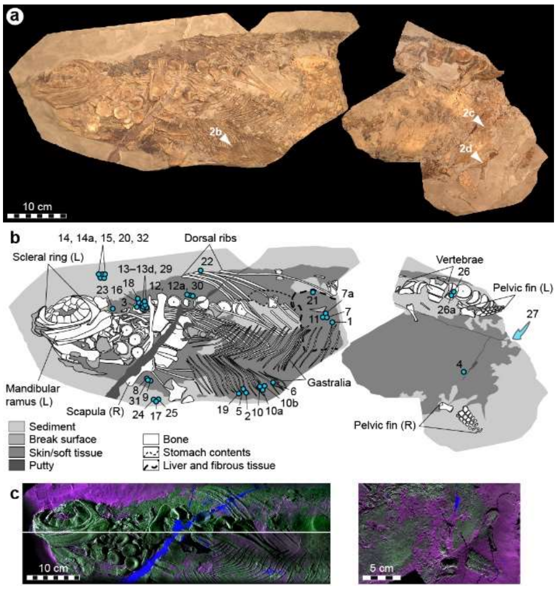

Figure 1 | *Stenopterygius* specimen MH 432. a, Photographic and **b**, diagrammatic representation of the fossil in oblique ventral view. Arrowheads indicate enlargements in Fig. 2; numerals (blue circles) denote sample locations (Sample 27 was taken from the underside of the slab). 'L' and 'R' indicate left- and right-hand skeletal elements. **c**, SRS-XRF false-colour images showing the spatial distribution of potassium (magenta), calcium (green) and titanium (blue). Extended Data Fig. 1 presents additional SRS-XRF maps and photographs of MH 432 under regular and UV light.

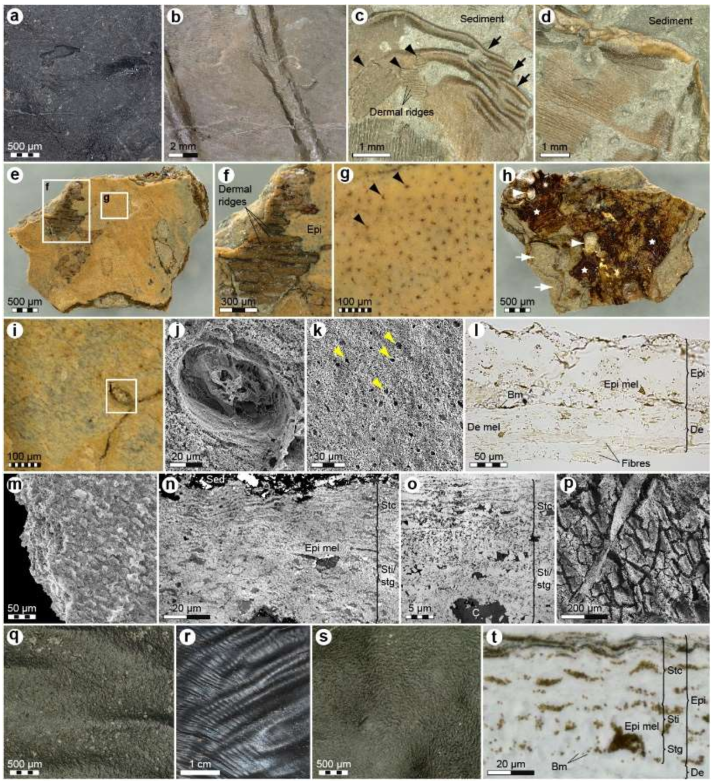

Figure 2 | Fine structure of *Stenopterygius* specimen MH 432 integument. a, External aspect of untreated epidermis (Sample 13) showing absence of scales (compare Fig. 2q, s). **b**, Skin adhering to the gastralia. **c**, Folding (arrows) and fragmentation (arrowheads) of the integument (compare Fig. 2r). **d**, Trailing edge of the right pelvic fin with *post mortem* rippling. **e**, Exterior of demineralised flank integument (Sample 13a). **f**, Enlargement of interdigitating epidermal and dermal ridges. Epi, epidermis. **g**, Magnified image of subsurface melanophores (arrowheads) embedded in the semi-transparent epidermis. **h**, Internal aspect of demineralised integument showing remnants of blubber and underlying connective tissue (stars). Arrows = infiltrating sediment; arrowheads = authigenic silica minerals. **i**, Demineralised belly skin surface (Sample 10) lacking epidermal melanophores (compare Fig. 2g). **j**, FEG-SEM micrograph of a potential pore. **k**, Fractured stratum corneum (Sample 13a) with presumed lipid inclusions preserved as cavities (arrowheads). **l**, LM section through stratified skin (Sample 12a) (compare Fig. 2t). Bm, basement membrane; De, dermis; De mel, dermal melanophore; Epi mel, epidermal melanophore. **m**, Oblique transverse section through the stratum corneum (Sample 10). **n**, TEM section through pigmented epidermis (Sample 13). Sed, sediment; Stc, stratum corneum; Sti/stg, stratum intermedium/stratum germinativum. **o**, TEM section through unpigmented epidermis (Sample 10). C, cavity. **p**, FEG-SEM micrograph of dermal fibres in external view (Sample 13). **q**, *Delphinus delphis* skin surface. **r**, *Post mortem* deformation of *D. delphis* skin. **s**, Scaleless adult *Dermochelys coriacea* carapace skin. **t**, LM section through juvenile *D. coriacea* carapace skin.

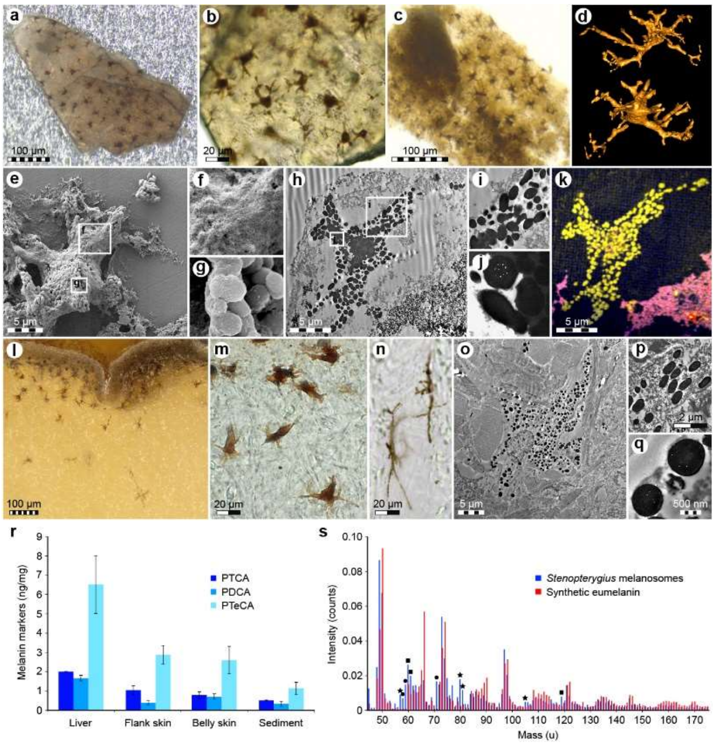

Figure 3 | Melanophores, melanosomes and eumelanin associated with MH 432. a, Light micrograph of epidermal melanophores embedded in semi-transparent phosphatic matrix (Sample 13b). **b**, Enlargement of fossil pigment cells and their branching processes (compare Fig. 3m). **c**, Melanophores retained in soft and pliable organic matter following demineralisation (Sample 13). **d**, SRXTM rendering of a melanophore with dendritic processes (Sample 18). **e**, FEG-SEM micrograph of a melanophore liberated from demineralised skin (Sample 13). **f**, Magnified outer membrane. **g**, Enlargement showing stacked melanosomes. **h**, TEM micrograph of a branched melanophore containing melanosome organelles surrounded by matrix (Sample 13; compare Fig. 3o). **i**, Magnified cellular extension with dispersed melanosomes (compare Fig. 3p). **j**, Enlargement showing internal melanosome vacuoles (compare Fig. 3q). **k**, False-colour negative ion NanoSIMS image illustrating the spatial distribution of CH^- (blue), CN^- (yellow) and S^- (red) (see Extended Data Fig. 3e). **l–q**, Melanophores in *Dermochelys coriacea* integument imaged under identical conditions as the ichthyosaur pigment cells. Flattened melanophores in **n** straddle a superficial blood vessel. **r**, Quantification of eumelanin markers produced by chemical degradation of MH 432 samples 7a (liver), 13a, d (flank skin), 10a, b (belly skin), and 14a (sediment) (see Extended Data Fig. 3f). **s**, Negative ion ToF-SIMS spectra obtained from sectioned MH 432 melanosomes and synthetic eumelanin (see Supplementary Information). Fossil spectrum peaks not consistent with eumelanin represent inorganic ions (squares), epoxy (circles) and sulfur-containing organic ions (stars).

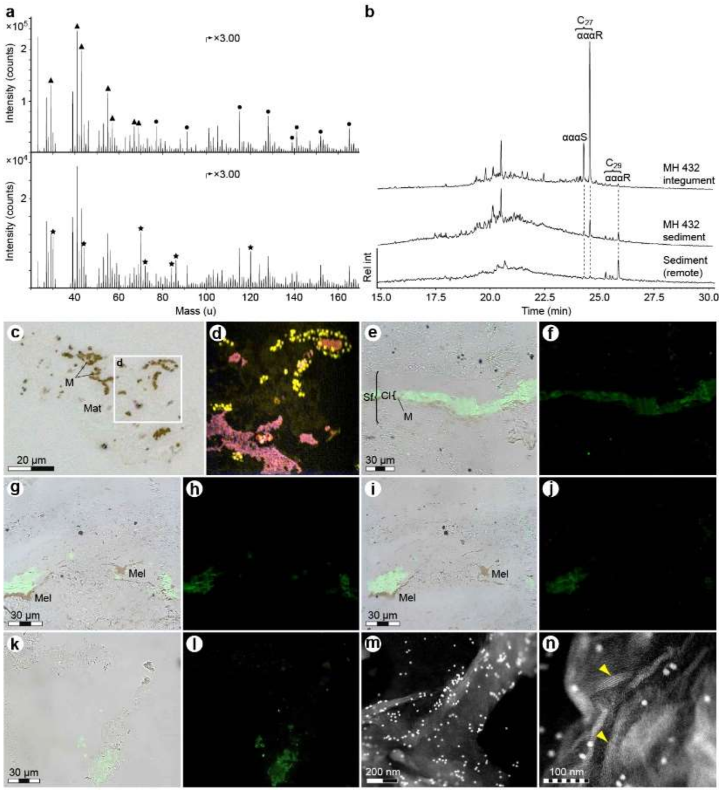

Figure 4 | Chemistry of MH 432 skin. a, Positive ion ToF-SIMS spectra featuring peaks characteristic of aliphatic and polyaromatic hydrocarbons (triangles and circles in spectrum at top; Sample 2), and proteinaceous compounds (stars in spectrum at bottom; Sample 13) (see Extended Data Fig. 5a, b). **b**, Py-GC/MS ion chromatograms (m/z 217, normalised to sample weight) revealing eukaryote-derived steranes from the integument (Sample 16), host rock (Sample 14) and sediment sampled at distance from the fossil (see Extended Data Fig. 4a). C_{27} (cholestanes), high in the integument, are interpreted as diagenetic products of ichthyosaur cholesterol. C_{29} (stigmastanes), pronounced in the sediment, represent background signal from algae and/or terrestrial plants. αααS and αααR = 5α,14α,17α(H) 20S and 20R isomers, respectively. **c**, LM section and **d**, false-colour negative ion NanoSIMS image illustrating the spatial distribution of CH^- (blue), CN^- (yellow) and S^- (red) (see Extended Data Fig. 2h). M, melanosomes; Mat, skin matrix. **e–l,** Immunohistochemical staining of demineralised MH 432 skin material exposed to antisera raised against: **e**, **f**, *Gallus domesticus* tropomyosin (Sample 13); **g**, **h**, *Alligator mississippiensis* and **i**, **j**, *Struthio camelus* haemoglobin (Sample 13); **k**, **l**, *G*. *domesticus* α-keratin (Sample 8). **e**, **g**, **i**, **k** indicate localisation of antibody-antigen complexes via superimposed green fluorescent signal on transmitted light images of sectioned tissue; **f**, **h**, **j**, **l** use a fluorescein isothiocyanate (FITC) filter. Both anti-haemoglobin antibodies have a similar binding pattern, and are localised to a discrete structure (vessel?) surrounded by a melanophore (compare Fig. 3n). Cl, concentration layer; Mel, melanophore; Sf, skin fold. **m**, Low- and **n**, high-magnification immunogold labelling of MH 432 skin fibres exposed to anti-α-keratin antibody (Sample 12). Arrowheads = filamentous matter (compare Extended Data Fig. 7s, t).

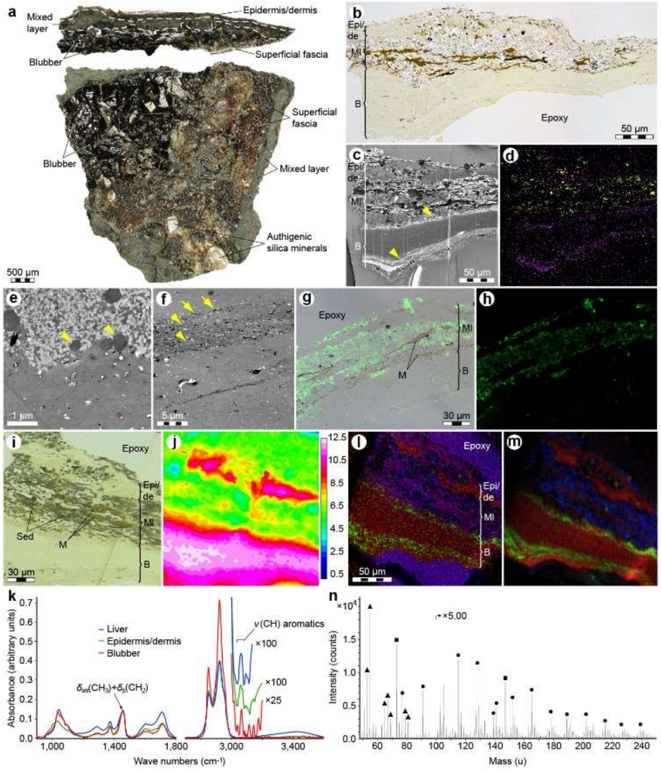

Figure 5 | Structure and chemistry of MH 432 blubber. a, Side (top) and internal (bottom) views of untreated integument (Sample 13a). Dashed line demarcates a layer containing both endogenous (skin) and exogenous (clay and bacteria) features (see Extended Data Fig. 10d–h). **b**, LM section through demineralised integument (Sample 13a). B, blubber; Epi/de, epidermis/dermis; Ml, mixed layer (see Supplementary Information). **c**, Backscattered electron micrograph and **d**, three-colour EDX map (Sample 13a) indicating the distribution of aluminium (lime), phosphorous (purple) and sulfur (yellow). Arrowheads = reticular dermis (top) and superficial fascia (bottom). **e**, TEM micrograph from the interface between the phosphatised epidermis/dermis (top) and polymerised blubber (bottom). Arrowheads = scattered melanosomes. **f**, Organic seams (arrowheads) with calcium phosphate nanocrystallites (arrows) embedded in amorphous blubber residue. **g**, **h**, Immunohistochemical staining for antibodies raised against α-keratin (green fluorescent signal) demonstrating absence of antibody-antigen complexes in the blubber (Sample 13a). M, melanosomes. **i**–**k**, IR absorbance data from the blubber (Sample 13a) along with spectra obtained from the epidermis/dermis (Sample 13a) and liver (Sample 1). Band assignments and vibration modes (as, asymmetric; *δ*, deformation; s, symmetric; *v*, stretching) are shown in **k**. Intensities in **j** originate from the 2,805–3,016 cm^{-1} interval denoting *v*(CH) absorption (see Supplementary Information). Sed, sediment (clay). **l**, Positive ion ToF-SIMS image of Sample 13a with peaks typical of polyaromatics (red), calcium phosphate (green) and epoxy (blue). **m**, Negative ion ToF-SIMS image with peaks characteristic of sulfur-containing fragments (red), phosphate (green) and silica (blue). **n**, Positive ion ToF-SIMS spectrum recorded from the blubber. Triangles and circles denote peaks typical of aliphatics and polyaromatics, respectively; squares = PDMS (see Supplementary Information).

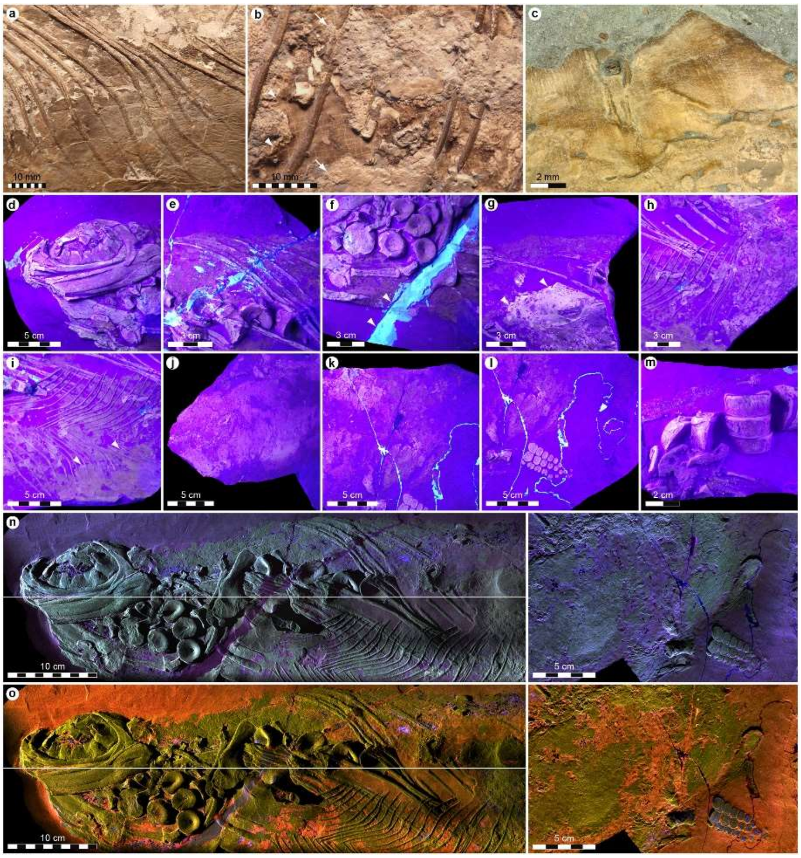

Extended Data Figure 1 | Regular, UV light and SRS-XRF images of MH 432. a, Skin compressed onto the diagenetically flattened gastralia basket. **b**, Amorphous adipocere (arrows) external to the gastralia and liver residue (arrowheads) within the abdominal cavity. **c**, Fibrous muscle or connective tissue on left side of the trunk. **d–m**, Certain anatomical features, and the stone putty used to reassemble the individual blocks, are enhanced under UV light. Note differences in fluorescence between the putty (arrowheads in **f**), internal structures (arrowheads in **g**) and integument (arrowheads in **i**). **n**, SRS-XRF false-colour images showing the spatial distribution of silicon (magenta), phosphorous (green) and copper (blue). **o**, SRS-XRF false-colour images showing the spatial distribution of iron (red), sulfur (yellow) and zinc (blue). The lack of co-localisation between copper, zinc and the preserved soft tissues might result from calcium phosphate overprinting.

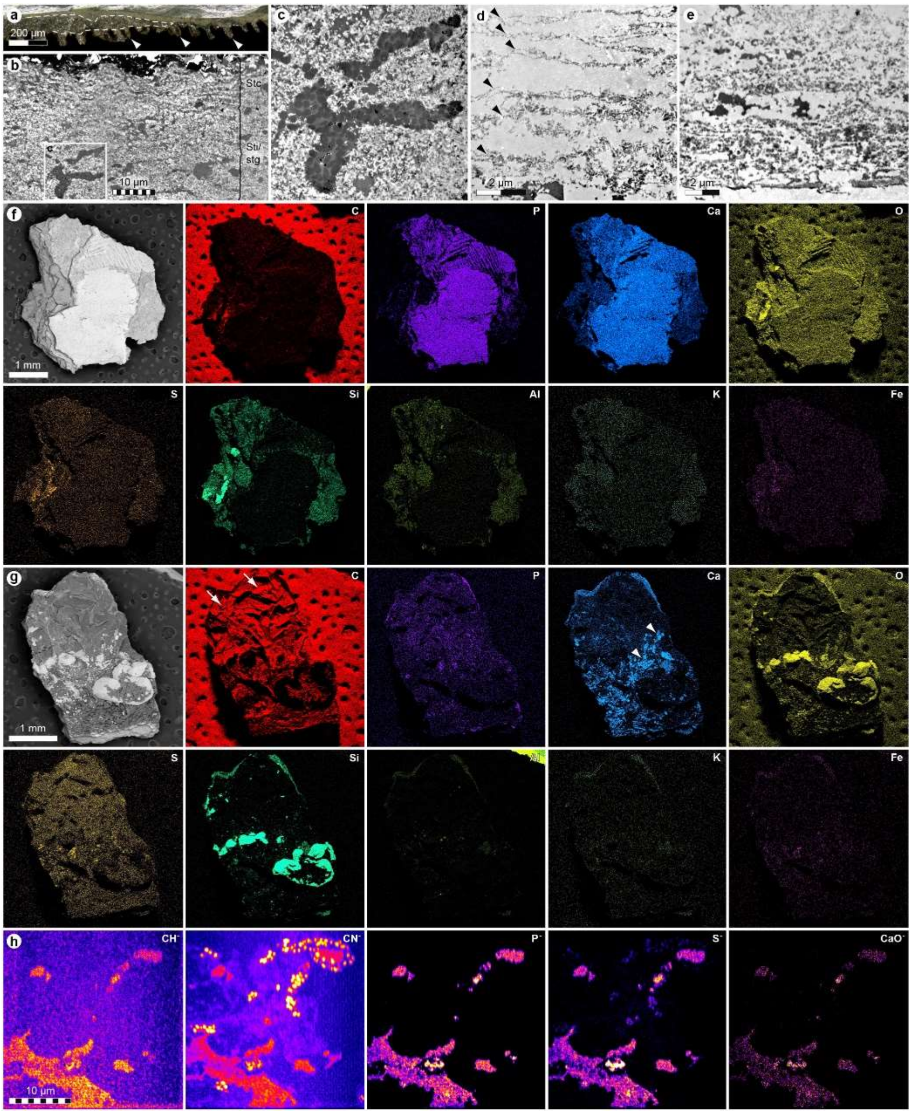

Extended Data Figure 2 | LM, TEM, EDX, and NanoSIMS data from MH 432 integument. **a**, Transverse section through demineralised epidermis (Sample 13a) showing epidermal ridges (arrowheads) and invasive sediments (dashed line). **b**, TEM micrograph through the stratified epidermis (Sample 13). Stc, stratum corneum; Sti/stg, stratum intermedium/stratum germinativum. **c**, Enlargement of a branched epidermal melanophore. **d**, Squamous keratinocytes from between the stratum intermedium and stratum corneum (Sample 10); these become progressively flattened towards the exterior surface (top). Arrowheads = cellular envelopes. **e**, TEM section through the fibrous superficial dermis (Sample 12a). **f**, Backscattered electron micrograph and single-element EDX maps of untreated integument in external view. Coloured images illustrate the relative abundance of each element, with higher intensities indicating greater abundance. Note enrichment of calcium and phosphorous in the fossilised epidermis and dermis. Intensities from carbon derive primarily from the underlying conductive tape. Al, aluminium (lime); C, carbon (red); Ca, calcium (blue); Fe, iron (violet); K, potassium (turquoise blue); O, oxygen (yellow); P, phosphorous (purple); S, sulfur (orange); Si, silicon (turquoise). **g**, Backscattered electron micrograph and single-element EDX maps of untreated integument in internal view (colours as in **f**). Note high levels of carbon (arrows) and localised enrichment of calcium (arrowheads) in the blubber and subjacent fibrous tissue. Intensities from silicon and oxygen derive primarily from authigenic silica minerals. **h**, High-resolution NanoSIMS images acquired from demineralised skin showing the distribution of CH$^-$, CN$^-$, P$^-$, S$^-$, and CaO$^-$ (Sample 13a). CN$^-$-rich microbodies are melanosomes (see Extended Data Fig. 3e).

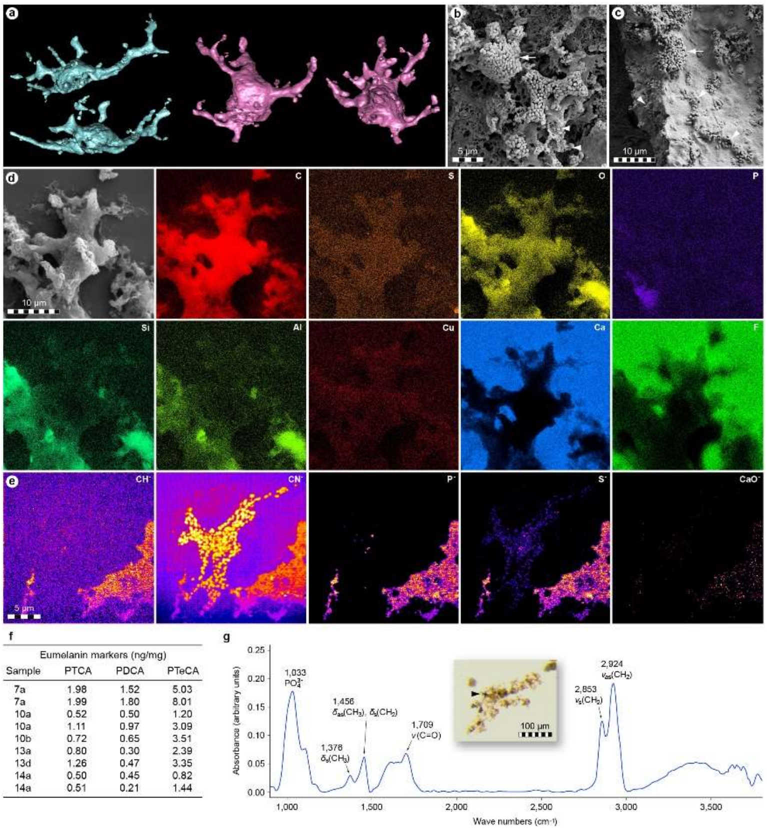

	Eumelanin markers (ng/mg)		
Sample	PTCA	PDCA	PTeCA
7a	1.98	1.52	5.03
7a	1.99	1.80	8.01
10a	0.52	0.50	1.20
10a	1.11	0.97	3.09
10b	0.72	0.65	3.51
13a	0.80	0.30	2.39
13d	1.26	0.47	3.35
14a	0.50	0.45	0.82
14a	0.51	0.21	1.44

Extended Data Figure 3 | Three-dimensional visualisation and chemistry of MH 432 melanophores. a, SRXTM renderings of branched melanophores (Sample 18). **b**, FEG-SEM micrograph of a dermal melanophore and adjacent organic matter recovered from demineralised integument (Sample 13a). Note remnant cell body (arrow) and external moulds of disrupted pigment organelles in the polymerised matrix of one dendrite (arrowheads). **c**, FEG-SEM micrograph of a dermal melanophore and adjacent organic matter from demineralised integument (Sample 13). Note clustered melanosomes representing the cell body (arrow) and dendritic extensions packed with pigment organelles (arrowheads). **d**, Backscattered electron micrograph and single-element EDX maps of the melanophore in Fig. 3e–g. Coloured images illustrate the relative abundance of each element, with higher intensities indicating greater abundance. Note enrichment of carbon and, to a lesser extent, sulfur and oxygen in the fossil pigment cell. Intensities from calcium and fluoride derive from the underlying spectrophotometric window (see Extended Data Fig. 3g). Al, aluminium (lime); C, carbon (red); Ca, calcium (blue); Cu, copper (dark red); F, fluoride (green); O, oxygen (yellow); P, phosphorous (purple); S, sulfur (orange); Si, silicon (turquoise). **e**, High resolution NanoSIMS images of the melanophore in Fig. 3h–k showing the distribution of CH^-, CN^-, P^-, S^-, and CaO^-. Note relatively high levels of CN^- and S^- in the melanosomes, whereas the surrounding matrix also contains measurable amounts of CH^- and P^-. **f**, Alkaline hydrogen peroxide oxidation products PTCA, PDCA and PTeCA (Fig. 3r) from samples 7a (two batches), 10a (two batches), 10b, 13a, 13d, and 14a (two batches). **g**, IR spectrum from the melanophore in Fig. 3e–g (arrowhead in the inset LM image) showing peaks attributed to hydrocarbons and phosphate.

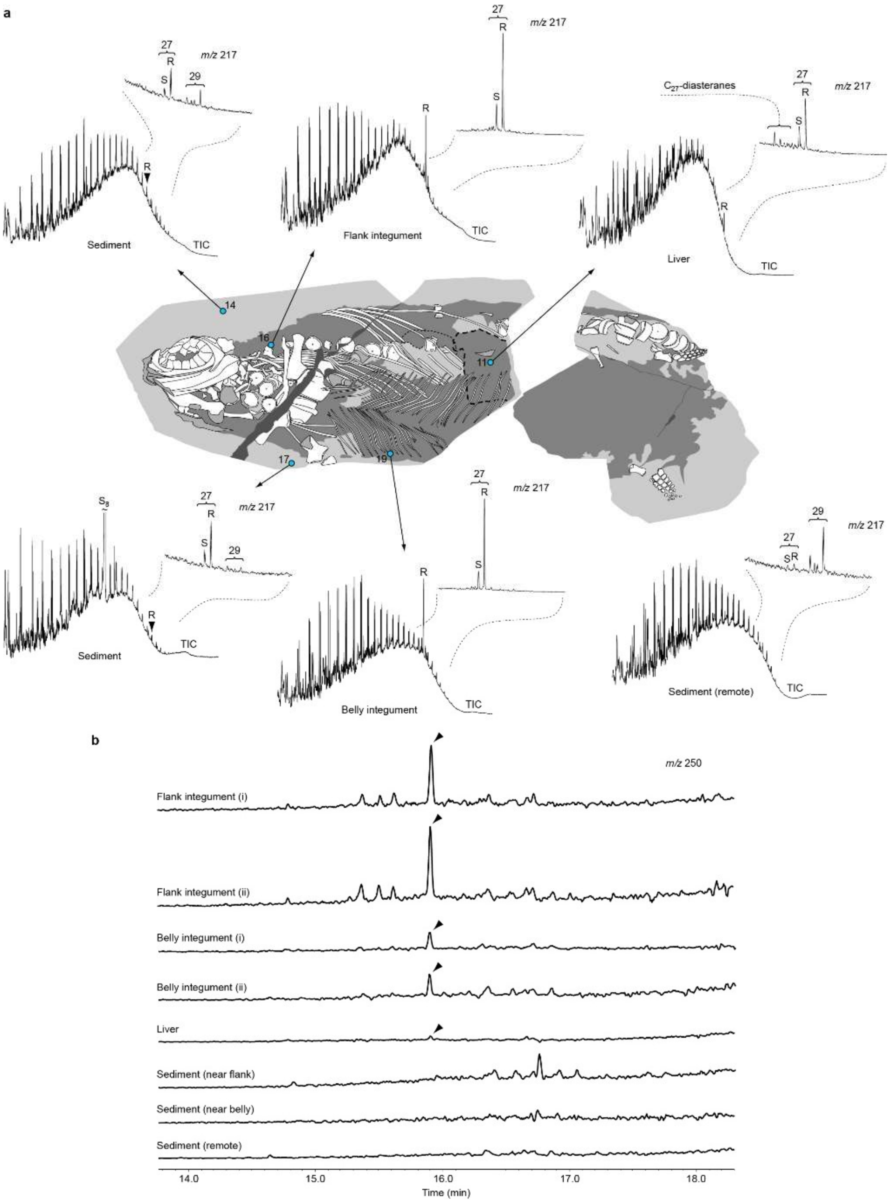

Extended Data Figure 4 | Pyrolysis data (560°C, 10 s) from MH 432 soft tissues. a, Py-GC/MS chromatograms obtained from MH 432 (TIC, total ion currents). The prominent peak series in each sample represents homologous *n*-alkenes/*n*-alkanes; chromatograms are normalised to the highest of these peaks. Inset ion chromatograms (m/z 217) illustrate the distribution of eukaryote-derived steranes, with '27' and '29' denoting carbon numbers. 'S' and 'R' = 5α,14α,17α(H) 20S and 20R isomers, respectively. Abundant C_{27}-steranes (cholestanes) in the integument constitute diagenetic products of ichthyosaur cholesterol. The predominant 20R isomer is also indicated in the TICs to illustrate its abundance among the total pyrolysates. C_{29}-steranes (stigmastanes) reflect background sedimentation from algae and/or terrestrial plants. Note high amount of cholestanes in the integument and greater abundance of stigmastanes in the host rock. Also note higher intensities of aromatics (relative to aliphatics), diasteranes (relative to regular steranes), and a stronger unresolved complex mixture in the liver, reflecting original compositional differences and/or enhanced biodegradation. **b**, Py-GC/MS ion chromatograms (m/z 250, normalised to sample weight) showing a compound tentatively identified as *n*-octadecadiene (n-$C_{18:2}$—arrowheads). This molecule is interpreted as a pyrolysis product of kerogen-bound *n*-octadecenyl (n-$C_{18:1}$) moieties potentially originating from oleic acid ($C_{18:1}\omega 9c$), the most abundant monoenoic fatty acid in extant vertebrates. Note the localised occurrence within the flank integument (where the blubber is best preserved). Replicate sample measurements (i, ii) are provided to demonstrate reproducibility.

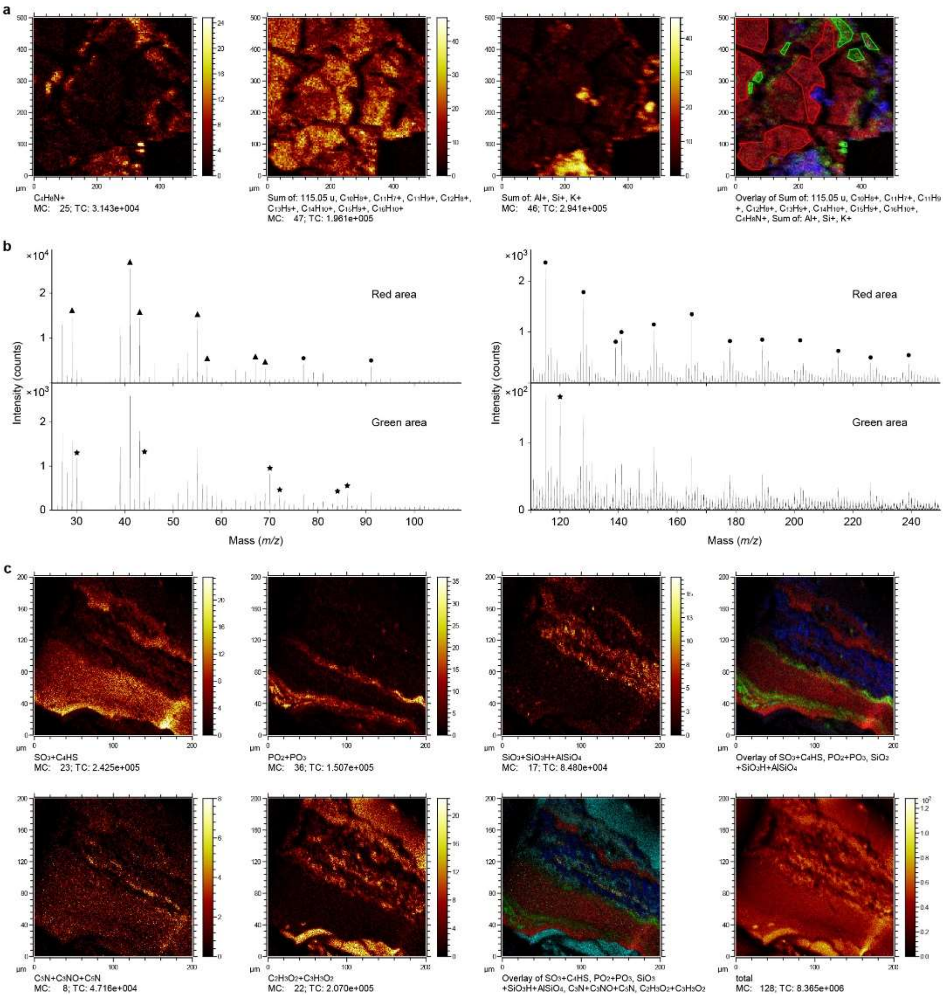

Extended Data Figure 5 | ToF-SIMS images and spectra from MH 432 integument. a, Images of positive ions (Sample 2) characteristic of (from left) peptides/proteins ($C_4H_8N^+$, 70 u), polyaromatic hydrocarbons, PAH ($C_9H_7^+$, 115 u; $C_{10}H_8^+$, 128 u; $C_{11}H_7^+$, 139 u; $C_{11}H_9^+$, 141 u; $C_{12}H_8^+$, 152 u; $C_{13}H_9^+$, 165 u; $C_{14}H_{10}^+$, 178 u; $C_{15}H_9^+$, 189 u; $C_{16}H_{10}^+$, 202 u), and the sedimentary matrix (Al^+, 27 u; Si^+, 28 u; K^+, 39 u), along with a three-colour overlay image of these ions where green represents proteinaceous matter, red PAH and blue sediment. **b**, Positive ion spectra from selected regions of interest (ROI) indicated in the three-colour overlay image in **a** (green demarcations highlight areas dominated by proteinaceous matter; red lines frame PAH-rich regions). Characteristic aliphatic and PAH peaks are indicated by triangles and circles, respectively, in the top spectrum (red ROI), whereas typical protein fragment ions are denoted by stars in the bottom spectrum (green ROI; see Supplementary Information). **c**, Negative ion images of Sample 13a (see Fig. 5m) representing (top row, from left) sulfur-containing materials (SO_3^-, 80 u; C_4HS^-, 81 u), phosphate (PO_2^-, 63 u; PO_3^-, 79 u) and the sedimentary matrix (SiO_3^-, 76 u; $SiHO_3^-$, 77 u; $AlSiO_4^-$, 119 u), together with a three-colour overlay image of these ions in red, green and blue, respectively. The bottom row shows the spatial distribution of ions representing eumelanin (C_3N^-, 50 u; C_3NO^-, 66 u; C_5N^-, 74 u) and epoxy ($C_2H_3O_2^-$, 59 u; $C_3H_3O_2^-$, 71 u), along with a five-colour overlay image featuring sulfur-containing ions (red), phosphate (green), eumelanin (yellow), epoxy (cyan), and sediment (blue); the total ion image is shown on the far right.

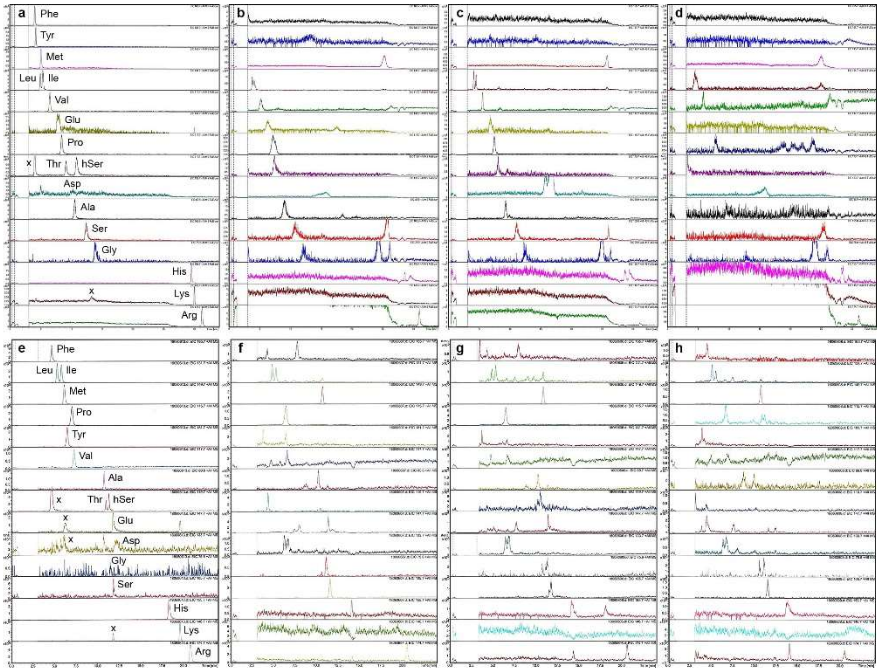

Extended Data Figure 6 | Amino acid analysis data from MH 432. a–**d**, LC condition I: **a**, Standard amino acids (200 pmol/4 μl). **b**, Sample 7a: liver (8.51 mg × 4 μl/170 μl). **c**, Sample 13d: integument (10.27 mg × 4 μl/206 μl). **d**, Sample 14a: sediment (10.05 mg × 4 μl/201 μl). **e**–**h**, LC condition II: **e**, Standard amino acids (200 pmol/4 μl). **f**, Sample 7a: liver (8.51 mg × 5 μl/340 μl). **g**, Sample 13d: integument (10.27 mg × 5 μl/411 μl). **h**, Sample 14a: sediment (10.05 mg × 5 μl/402 μl). Chromatograms for the unstable amino acids asparagine, cysteine, glutamine, and tryptophan were omitted from the figure. Additionally, aspartic acid, methionine and tyrosine were not detected (either due to their low ionisation efficacy or lability). Peaks with retention times similar to those of glycine and serine in the condition II chromatograms derive from impurities (as demonstrated by the corresponding amino acid peaks in the condition I chromatograms). Data from condition I were used for alanine, glutamic acid, glycine, and serine; data from condition II for all other amino acids. Ala, alanine; Arg, arginine; Asp, aspartic acid; Glu, glutamic acid; Gly, glycine; His, histidine; hSer, homoserine; Ile, isoleucine; Leu, leucine; Lys, lysine; Met, methionine; Phe, phenylalanine; Pro, proline; Ser, serine; Thr, threonine; Tyr, tyrosine; Val, valine. x = impurity.

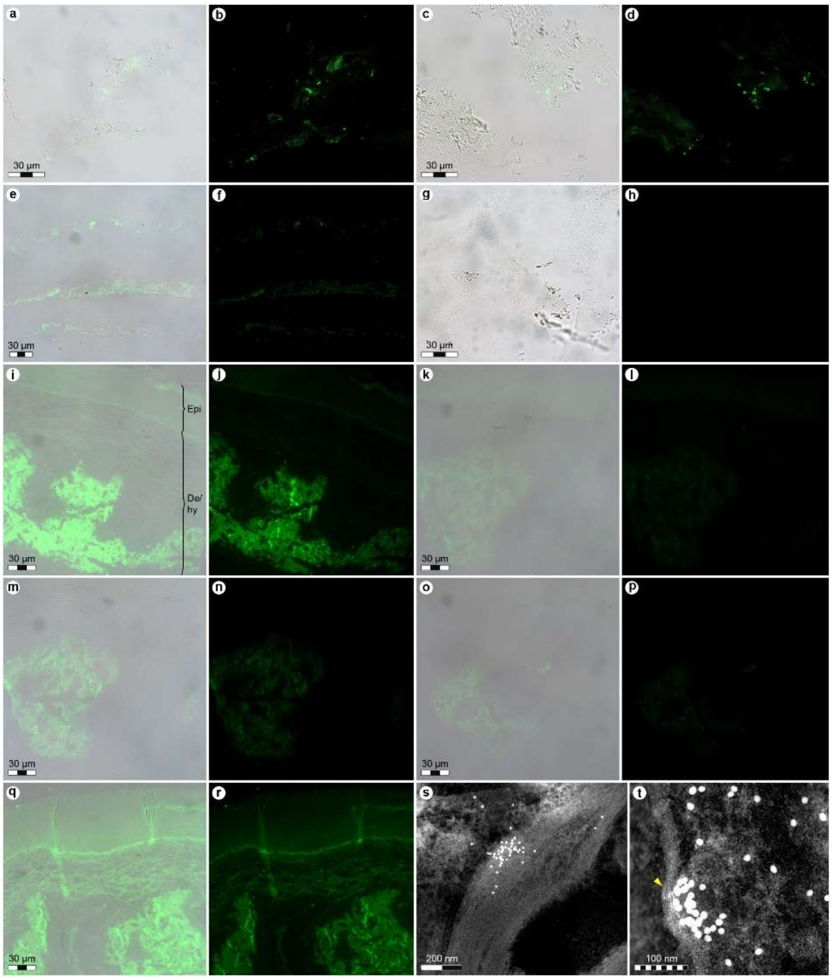

Extended Data Figure 7 | Immunoreactivity of fossil ichthyosaur and extant leatherback sea turtle skin. a–**h**, Immunohistochemical staining of demineralised MH 432 skin (samples 8 and 12a) *versus* **i**–**t**, experimentally treated *Dermochelys coriacea* skin exposed to antibodies raised against: **a**, **b**, *Bos taurus* elastin; **c**, **d**, *Gallus domesticus* actin; **e**, **f**, **k**, **l**, *Alligator mississippiensis* collagen; **g**, **h**, *G. domesticus* feathers (indicative of β-keratin); **i**, **j**, *G. domesticus* tropomyosin; **m**, **n**, *A. mississippiensis* haemoglobin; **o**, **p**, *Struthio camelus* haemoglobin; **q**–**t**, *G. domesticus* α-keratin. **a**, **c**, **e**, **g**, **i**, **k**, **m**, **o**, **q** show where the antibodies bind to tissue (green) superimposed on transmitted light images. FITC label fluorescence in **b**, **d**, **f**, **h**, **j**, **l**, **n**, **p**, **r** indicates binding for all antibodies except β-keratin. Migration of α-keratin-derived compounds from the epidermis to underlying tissues in *D. coriacea* likely reflects the combined effects of decay, compaction and maturation. De/Hy, dermis/hypodermis (corresponding to blubber in adult *D. coriacea*); Epi, epidermis. **s**, Low and **t**, high resolution localisation of anti-α-keratin antibody tagged with gold to fibrous matter in *D. coriacea* skin. Note filamentous structures (arrowhead).

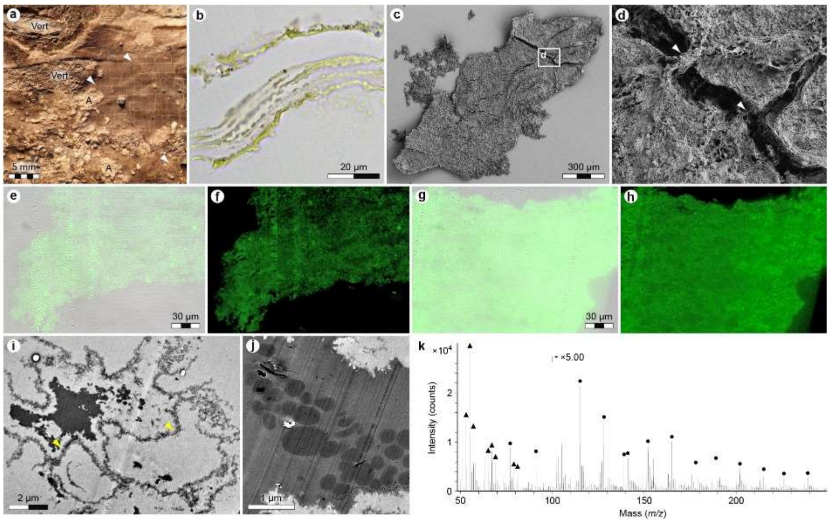

Extended Data Figure 8 | Ultrastructure and chemistry of MH 432 liver. **a**, Polygonal surface structure of the red-brown organ trace (arrowheads). Note irregular patches of phosphatised adipocere (A) overlying the mineralised internal structure, and a vertebral centrum (Vert) that has penetrated the decomposing tissue prior to fossilisation. **b**, LM section through demineralised liver matrix (Sample 1) revealing its layered architecture (probably produced by diagenetic compaction). **c**, FEG-SEM micrograph of pliable organic matter released via treatment with EDTA (Sample 1). **d**, Enlargement showing a degraded and somewhat fibrous (arrowheads) biomass. **e**, **g**, Overlay and **f**, **h**, fluorescent images of demineralised liver material (Sample 7) exposed to antibodies raised against **e**, **f**, *Alligator mississippiensis* and **g**, **h**, *Struthio camelus* haemoglobin. **i**, TEM micrograph of probable cellular membranes (arrowheads). **j**, TEM micrograph showing a dense melanosome cluster (Sample 1). **k**, Positive ion ToF-SIMS spectrum with peaks characteristic of aliphatics (triangles) and polyaromatics (circles; Sample 1).

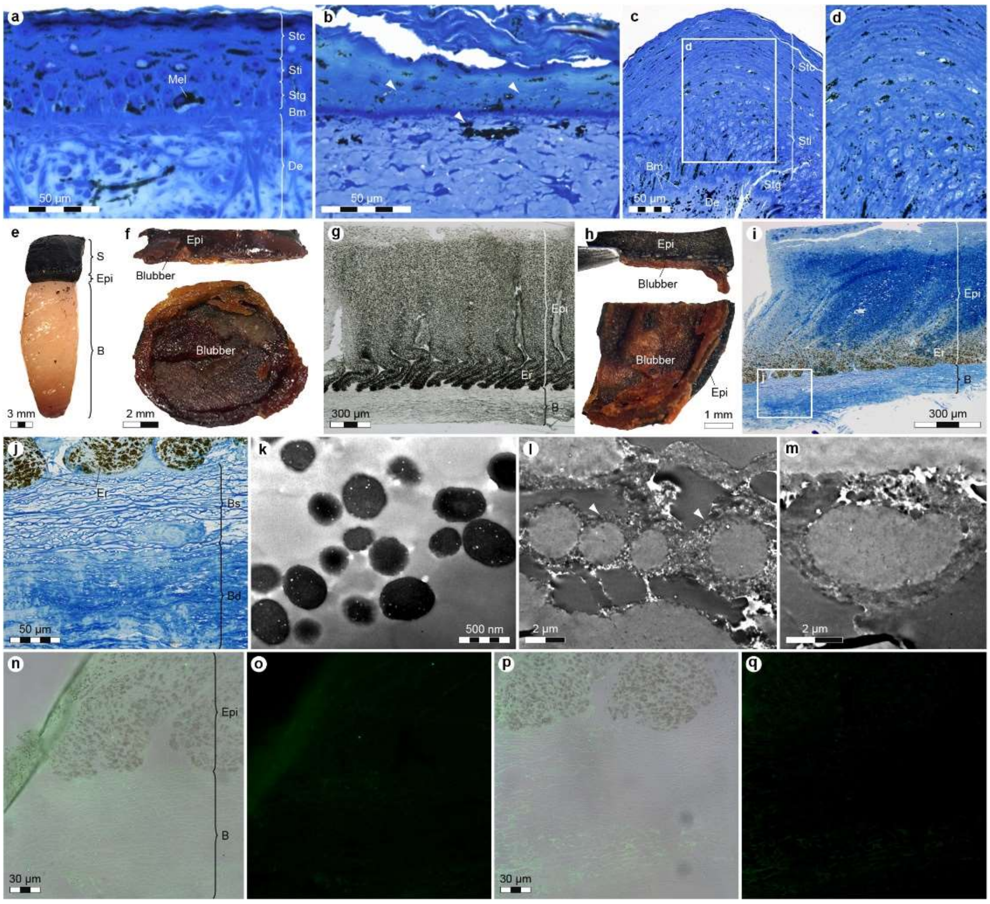

Extended Data Figure 9 | Experimental maturation of extant skin and subcutis to simulate the effects of diagenesis. a, Stained LM section through the scaly carapace integument from a juvenile *Dermochelys coriacea*. Bm, basement membrane; De, dermis; Mel, melanophore; Stc, stratum corneum; Stg, stratum germinativum; Sti, stratum intermedium. **b**, Autoclave treated juvenile *D. coriacea* carapace integument showing flattened keratinocytes and melanophores (arrowheads). **c**, Scaleless carapace integument of an adult *D. coriacea* revealing multiple layers of stratified squamous keratinocytes. Note greater thickness of the stratum intermedium relative to the juvenile individual (compare Extended Data Fig. 9a). **d**, Enlargement of stratum corneum and stratum intermedium. **e**, Melanised *Phocoena phocoena* body integument. B, blubber (dermis and subcutis); Epi, epidermis; S, outer skin surface (in oblique aspect). **f**, Lateral (top) and internal (bottom) views of artificially compressed *P. phocoena* integument. **g**, LM section through artificially compressed *P. phocoena* integument showing condensed blubber layer (compare Extended Data Fig. 9e). Er, epidermal ridge. **h**, Lateral (top) and internal (bottom) views of *P. phocoena* integument following autoclave experiments. **i**, Stained LM section through autoclave treated *P. phocoena* integument. **j**, Enlargement of the loosely packed superficial blubber (Bs) – a possible entry for microbes (compare Extended Data Fig. 10d) – and dense deeper blubber (Bd). **k**, Melanosomes in experimentally treated *P. phocoena* epidermis. **l**, **m**, Shrunken, membrane bound (arrowheads) adipocytes (or lipid vesicles) in experimentally treated *P. phocoena* blubber (compare Extended Data Fig. 10g). **n**, **p**, Overlay and **o**, **q**, fluorescent images of experimentally treated *P. phocoena* integument exposed to antibodies raised against: **n**, **o**, *Gallus domesticus* α-keratin; **p**, **q**, *G. domesticus* tropomyosin.

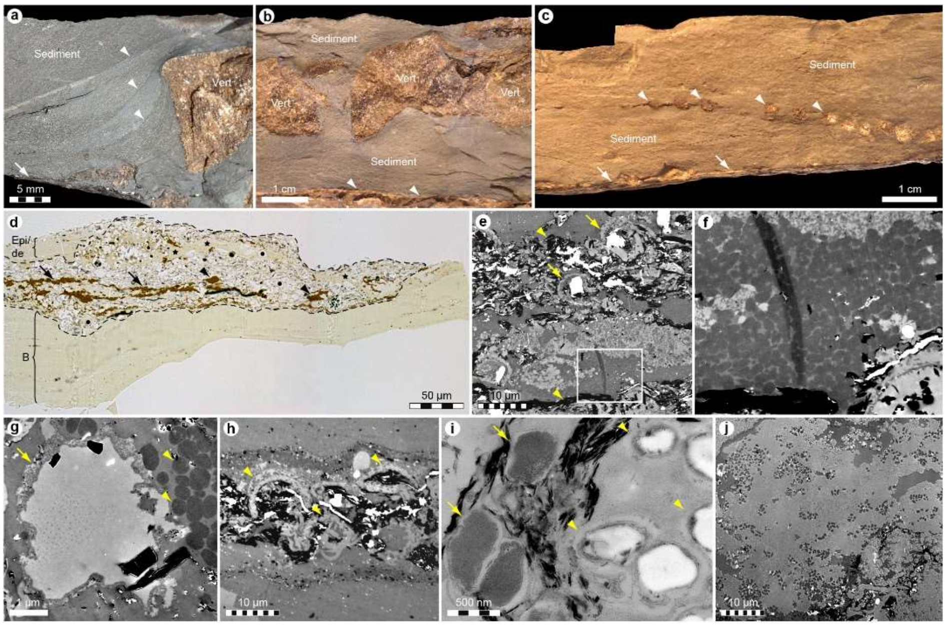

Extended Data Figure 10 | Taphonomy of MH 432. a, Cross-section through the main rock slab (left side of posterior termination) in original geological orientation showing sediment infill between the integument (arrow) and a sectioned vertebra (Vert). Saturated mud (arrowheads) encased the carcass following gravitational collapse of the backbone. **b**, Natural break through the main slab (centre of posterior termination) exposing intrusive sediment infill into the body cavity prior to disarticulation of the vertebral column. Arrowheads indicate the liver residue. **c**, Cross-section through the main slab (right side of posterior termination). Note invasive sediment covering the residual soft parts (arrows) and dorsal ribs from the right side of the body (arrowheads). **d**, LM section through demineralised integument (Sample 13a) with clay minerals and inferred bacteria (delimited by dashed line) penetrating between the phosphatised epidermis/dermis (Epi/de) and polymerised blubber (B). Skin (stars) and melanophores (arrowheads) occur along with hollow structures interpreted as bacterial cellular bodies (circles) and massed melanosomes (arrows). **e**, TEM micrograph of Sample 13a showing clay minerals (arrowheads) and bacterial cells (arrows). **f**, Enlarged melanosome concentration produced by microbially mediated skin reduction. **g**, Adipocyte/vesicle (compare Extended Data Fig. 9l, m) or microbe (compare Extended Data Fig. 10i) with well-developed cellular membrane (arrow) and adjacent melanosomes (arrowheads). **h**, Collapsed thick-walled bacterial cells (arrowheads) suggesting microorganismal infestation prior to fossilisation and diagenetic compaction (Sample 13a). **i**, Comparative image of extant bone-boring bacteria (arrows) showing retention of cellular membranes (arrowheads) after removal of internal contents. **j**, Decomposed skin of MH 432 (Sample 13).